Mehdi Hatab, Bsc.

INVESTIGATING THE DARWIN APPROXIMATION WITH COMPLEX PERMEABILITY FOR THE SIMULATION OF FERRITE CHOKES

MASTER'S THESIS

submitted to

Graz University of Technology

Supervisors

Dipl.-Ing. Dr.techn Klaus Roppert

Institute of Fundamentals and Theory in Electrical Engineering

Graz, January 10, 2024

Affidavit

I declare that I have authored this thesis independently, that I have not used other than the declared sources/resources and that I have explicitly marked all material which has been quoted either literally or by content from the used sources.

date

(signature)

Acknowledgment

I would like to express my sincere gratitude to everyone who has contributed to the completion of this thesis. First and foremost, I would like to thank my thesis advisor Dipl.-Ing. Dr.techn Klaus Roppert for their guidance, support throughout this thesis.

I would like to thank my family for their unwavering love and support, which has been a constant source of inspiration for me. Lastly, I am grateful to all the researchers and authors whose works I have cited in this thesis for their contributions to the electromagnetic field.

Thank you all for being a part of this journey.

Abstract

This thesis presents an investigation of the Darwin approximation in the context of using ferrite chokes with complex permeability. Ferrite chokes play a critical role in electromagnetic compatibility (EMC) applications by mitigating common-mode (CM) and differential mode (DM) electromagnetic interference. The thesis begins with an introduction to the components of ferrite chokes, the CM and DM phenomena, and a discussion of the concept of complex permeability. A producer of an extraction technique, Iterative Rational Fraction Analysis (IRFA), is presented to extract the lumped-element equivalent of ferrite chokes. The Darwin approximation, a simplified representation of electromagnetic fields, i.e., an approach to Maxwell's equation that ignores the wave effect, is derived and then subjected to finite element analysis using (openCFS). In parallel, the full set of Maxwell's equations is simulated using CST Studio Suite to provide a basis for comparison. Finally, the impedance characteristics of CM and DM obtained by the Darwin approximation and the full set of Maxwell's equations are evaluated, highlighting the strengths and limitations of each approach.

Zusammenfassung

In dieser Arbeit wird die Darwin-Approximation im Zusammenhang mit der Verwendung von Ferritdrosseln mit komplexer Permeabilität untersucht. Ferritdrosseln spielen eine entscheidende Rolle in Anwendungen der elektromagnetischen Verträglichkeit (EMV), indem sie elektromagnetische Störungen im Gleich- und Gegentakt dämpfen. Die Arbeit beginnt mit einer Einführung in die Komponenten von Ferritdrosseln, die Gleichtakt- und Gegentaktphänomene und einer Diskussion des Konzepts der komplexen Permeabilität. Eine Extraktionstechnik, die Iterative Rationale Fraktionsanalyse (IRFA), wird vorgestellt, um die Ersatzschaltkomponenten von Ferritdrosseln zu extrahieren. Die Darwin-Approximation, eine vereinfachte Darstellung elektromagnetischer Felder, d.h. eine Approximation der Maxwell-Gleichung, die den Welleneffekt ignoriert, wird hergeleitet und einer Finite-Elemente-Analyse mit (openCFS) unterzogen. Parallel dazu wird die vollständige Maxwell-Gleichung mit der CST Studio Suite simuliert, um eine Vergleichsbasis zu schaffen. Schließlich werden die Gleichtakt- und Gegentaktimpedanzen, die mit der Darwin-Approximation und der vollständigen Maxwell-Approximation erhalten werden, bewertet, wobei die Grenzen jedes Ansatzes aufgezeigt werden.

CONTENTS

Contents i

List of Figures iii

List of Tables v

Glossary vii

1 Introduction **1**
- 1.1 Background 1
- 1.2 Motivation 2
- 1.3 Structure of the Thesis 2

2 Ferrite Chokes **3**
- 2.1 Chokes 3
- 2.2 Complex Permeability 4
- 2.3 Equivalent Circuit 4

3 Darwin approximation **11**
- 3.1 Introduction 11
- 3.2 Maxwell's Equation 12
- 3.3 Electric Field Decomposition 13
- 3.4 Magnetic Vector Potential 13
- 3.5 Electric Scalar Potential 14
- 3.6 Derivation of Darwin PDE 14
- 3.7 Finite Element Method 14
  - 3.7.1 Discretization 16

4 Choke Modeling **19**
- 4.1 Choke Model 19
- 4.2 Ferrite Permeability 20
  - 4.2.1 Fair-rite 75 20
  - 4.2.2 Fair-rite 98 20
  - 4.2.3 TDK T37 22

5 Simulation and Results **23**
- 5.1 openCFS 23
- 5.2 CST Studio Suite® 24
  - 5.2.1 Low-Frequency Solver 24
  - 5.2.2 High-Frequency Solver 26

5.3 Results 27
5.3.1 Common-Mode Choke 27
5.3.2 Differential-Mode Choke 29
5.3.3 Passivity 30

Conclusion **37**

A Appendix A **39**
A.1 Stability 39
A.2 Passivity 39

B Appendix B **41**
B.1 MATLAB code 41

Bibliography **45**

List of Figures

4.1 Ferrite Choke (all dimension in mm). 19
4.2 Complex permeability of Fair-rite 75 material. 21
4.3 Complex permeability of Fair-rite 98 material. 21
4.4 Complex permeability of TDK T37 material. 22

5.1 Boundary condition for Darwin model solver. 25
5.2 Current port in CST. 25
5.3 Discrete Port. 27
5.4 Impedance of the CM choke using Fair-rite 75. 28
5.5 Impedance of the CM choke using Fair-rite 98. 28
5.6 Impedance of the CM choke using TDK T37. 29
5.7 The equivalent circuit of the CM choke using Fair-rite 75. 30
5.8 The equivalent circuit of the CM choke using Fair-rite 98. 31
5.9 The equivalent circuit of the CM choke using TDK T37. 31
5.10 Impedance of the DM choke using Fair-rite 75. 32
5.11 Impedance of the DM choke using Fair-rite 98. 32
5.12 Impedance of the DM choke using TDK T37. 33
5.13 The equivalent circuit of the DM choke using Fair-rite 75. 34
5.14 The equivalent circuit of the DM choke using Fair-rite 98. 35
5.15 The equivalent circuit of the DM choke using TDK T37. 35
5.16 Real component of $Y(s)$. 36

A.1 Linear-Time-Invariant system. 39

LIST OF TABLES

2.1 Equivalent circuit synthesis for the admittance [23]. 9
2.2 Equivalent circuit synthesis for the impedance [23]. 9

3.1 Electromagnetic field quantities. 13

4.1 Material properties of Fair-rite 75. 20
4.2 Material properties of Fair-rite 98. 20
4.3 Material properties of TDK T37. 22

5.1 Poles of the admittance $Y(s)$. 33

GLOSSARY

CM Common-Mode. 1, 2, 3, 23, 24, 26, 27, 30

DM Differential-Mode. 1, 2, 3, 24, 26, 29, 30

EC Equivalent Circuit. 29

EMI Electromagnetic Interference. 1, 3, 8

FE Finite-Element. 11

FEA Finite-Element-Analysis. 1

FEM Finite-Element-Method. 4, 14, 15, 37

GA Genetic Algorithm. 1

IRFA Iterative Rational Function Approximation. 5, 6, 7, 8, 37, 42

LF Low-Frequency. 6

openCFS Coupled Field Simulation. 23, 27

PDE Partial Differential Equation. 14, 15, 16

RFA Rational Function Approximation. 5, 6, 7, 42

Chapter

1

Introduction

1.1 Background

The electric drive system generates Electromagnetic Interference (EMI), including conductive, inductive, capacitive, and radiation types. One effective method to mitigate this noise is by incorporating a ferrite choke into the system, which suppresses both Common-Mode (CM) and Differential-Mode (DM) noises [4]. Typically, chokes are designed using toroid ferrite cores. Utilizing simulation models has been demonstrated to offer a more efficient approach for designing and testing ferrite chokes in comparison to the time- and resource-intensive physical manufacturing processes required for prototyping the product. In a study by [17], the authors utilized the high-frequency solver in CST to model a choke and compared its impedances with measured values. This methodology enabled them to analyze the parameters and their influence on the behavior of common-mode current in the choke. The S-parameters facilitated the extraction of common mode impedance, differential mode impedance, and inter-winding impedance in a single simulation. Furthermore, [5] discussed the recognition by the magnetostatic solver that not all magnetic flux compensates within the core of the DM choke, leaving some leakage flux. To address this, a simplified three-dimensional (3D) model of the CM choke was developed for Finite-Element-Analysis (FEA) of the magnetic field distribution. This 3D model replaced two continuous N-turn helical windings with two separate one-turn coil windings, considerably simplifying the realization of the finite element model. In a separate work, [16] presented an equivalent circuit of the ferrite choke as a parallel RLC with a resistor in series with the capacitor. At low frequencies, the impedance of a normal parallel RLC is typically almost zero due to the inductor functioning as a short circuit. However, beyond the resonance frequency at high frequencies, the impedance rapidly drops. To address this, a second resistor is introduced in series with the capacitor to mitigate the rapid impedance decrease after the resonance frequency. It is important to note that the discussed equivalent circuit is only for a single stage, leading to discrepancies at higher frequencies (>5MHz). To obtain the parameters, the process is carried out in two steps. The first step involves obtaining the coefficient of the rational function for the impedance (Z) using the (Levy's method). The second step entails deriving the RLC parameters from the coefficient using an optimization method. Care must be taken with the initial values of the RLC parameters during this process. In [22], a stochastic method, referred to as Genetic Algorithm (GA), was utilized to determine the parameters of the equivalent circuit. The circuit they proposed involves connecting parallel RLC circuits in series and includes parasitic capacitance between the winding at the circuit's ends. This method produce an accurate equivalent circuit. However, the algorithm's convergence time is typically long when dealing with a large search space.

1.2 Motivation

The thesis aims to investigate the numerical solution of the Darwin approximation via introducing the complex permeability using a ferrite choke. The Darwin approximation allows for the evaluation of the effects of inductance, capacitance, and resistance,while neglecting the wave effect, in contrast to the magneto-quasistatic (eddy current problem), which only considers the behavior of inductance and resistance. Meanwhile, in electro-quasistatic consider the behavior of the capacitance and resistance. The electric and magnetic energy densities are taken into consideration for further classification. In the case where the electric energy density is significantly greater than the magnetic energy density throughout the problem domain, the electro-quasistatic model is applicable, and variations in the magnetic field can be ignored. This results in an irrotational electric field governed by resistive and capacitive effects. Conversely, in situations where the magnetic energy density is much larger than the electric energy density, the magneto-quasistatic field approximation is utilized, focusing on resistive and inductive field effects while neglecting displacement currents in Ampere's law. When the electric and magnetic energy densities are approximately equal, all capacitive, resistive, and inductive field effects are taken into account and using Darwin model [7].

1.3 Structure of the Thesis

Chapter 2 discusses the use of ferrite chokes, including CM chokes and DM chokes. It also explains the complex permeability of the ferrite chokes. Finally, a process is introduced to obtain the lumped elements of the equivalent circuit of a ferrite choke. Chapter 3 discusses the Darwin approximation and the necessary conditions to derive it from the complete set of Maxwell's equations. In this chapter, also the finite element analysis of the Darwin approximation is presented. Chapter 4 discusses the choke model, that will be utilized for simulation purposes. Chapter 5 discusses the software used for simulating the Darwin approximation (openCFS) and for solving Maxwell's equations (CST studio suite). The chapter also discusses the boundary conditions for each software. Finally, the chapter presents the simulation and the equivalent circuit results for the CM and DM impedance.

CHAPTER 2

Ferrite Chokes

2.1 Chokes

Chokes are an essential component of EMI filters that are used to filter out EMI emissions in power supplies and motor drive systems. These filters effectively suppress both CM and DM noise. Chokes can work as CM and DM chokes. Common mode noise occurs when unwanted signals (voltage, current), usually from external sources, are introduced into a circuit or system in phase and at the same amplitude. This type of interference can result from power lines, ground loops, or electromagnetic induction [18]. When common noise arises in the differential pair, it initiates magnetic flux in both windings of the common mode choke. The windings of the common mode choke core are designed to merge the induced magnetic flux produced by one line's noise with the magnetic flux created by the other line, ultimately generating a rotating magnetic field (as depicted in Figure 2.1). The common mode choke functions as an inductor that impedes the noise frequency, enabling lower frequencies to pass while damping high-frequency noise. Differential mode noise, on the other hand, occurs when unwanted signals are introduced into a circuit or system in anti-phase and at the same amplitude. These disturbances typically result from internal sources such as the switching components within the inverter, power supply fluctuations [18]. A differential mode choke is utilized to eliminate differential mode noise, which damping high-frequency AC noise while permitting DC or low-frequency AC. If the currents of the differential signal in the signal pair flow in opposite directions, each line induces a magnetic flux of equal magnitude but opposite polarity to the other line, resulting in the cancellation of induced magnetic fluxes. As a result, the differential signal can pass with minimal attenuation, as illustrated in Figure 2.2

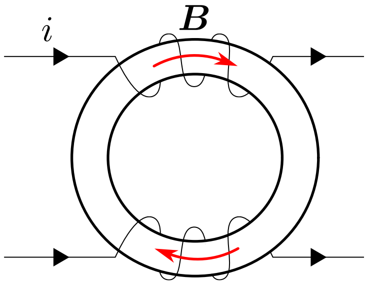

Figure 2.1: Magnetic field for the case CM.

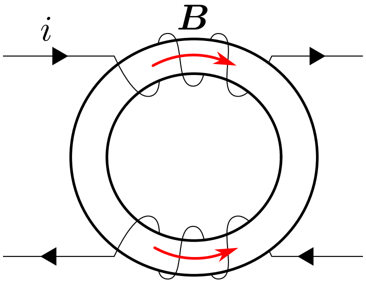

Figure 2.2: Magnetic field for the case DM.

2.2 Complex Permeability

Magnetic permeability measures a material's capacity to conduct a magnetic field and is quantified as the ratio of magnetic flux density to magnetic field intensity. Complex permeability, by disparity, contains real and imaginary components that are frequency-dependent. The real component relates to inductance, responsible for energy storage, when there is a magnetic field. Meanwhile, the imaginary component relates to the core loss, due to hysteresis loss, eddy-current loss and excess loss [19]. When a ferrite material is subjected to an alternating magnetic field of $H(t) = \hat{H}e^{j\omega t}$, the corresponding flux density $B(t)$ experiences a phase shift of angle δ due to losses. $(B(t) = \hat{B}e^{j\omega t - j\delta})$.

$$\bar{\mu} = \frac{B(t)}{H(t)} = \frac{\hat{B}e^{j\omega t - j\delta}}{\hat{H}e^{j\omega t}} = \frac{\hat{B}}{\hat{H}}e^{-j\delta} = \frac{\hat{B}}{\hat{H}}\cos\delta - j\frac{\hat{B}}{\hat{H}}\sin\delta = \mu_0(\mu' - j\mu'') = \mu_0\hat{\mu} \tag{2.1}$$

μ' characterizes the $B(t)$ component that is in phase with $H(t)$ and μ'' characterizes the $B(t)$ component that is delayed by $\pi/2$ phase-angle from $H(t)$ [19]. The expression for the impedance of an inductor utilizing a relative complex permeability $\hat{\mu}$ (dimensionless) can be stated as:

$$Z = j\omega\hat{\mu}L_0 = j\omega L_0(\mu' - j\mu''). \tag{2.2}$$

where L_0 represents the inductance of a coil in a vacuum. Consequently, this can be represented as a series circuit comprising of inductive L_s and resistive R_s elements:

$$Z = j\omega L_0(\mu' - j\mu'') = j\omega L_s + R_s. \tag{2.3}$$

Where L_s represents the magnetic energy storage $(\mu' L_0)$ and R_s represents the loss $(\mu''\omega L_0)$. Hence, the phase shift induced by magnetic losses is determined by:

$$\tan\delta = \frac{R_s}{\omega L_s} = \frac{\mu''}{\mu'} \tag{2.4}$$

2.3 Equivalent Circuit

An essential objective of deducing the parameters of a ferrite choke from Finite-Element-Method (FEM) analysis is to incorporate the derived ferrite choke into a circuit for additional assessment using tools like LTSpice or other circuit simulation software. This facilitates the examination of the influence of the modeled choke within the circuit, rather than attempting to simulate the entire setup using FEM.

In this chapter, the methodology from [23] is revisited due to consistency and readability considerations and the most important results from [23] are summarized. The extraction process was systematically carried out using the Rational Function Approximation (RFA) (Levy's technique [3]) approach, which employs an iterative scheme known as Iterative Rational Function Approximation (IRFA). This technique facilitates the efficient and accurate derivation of the circuit parameters.

The estimated impedance can be expressed as a transfer function:

$$Z_{\text{fit}}(s) = \frac{B(s)}{A(s)} = \frac{b_m s^m + b_{m-1} s^{m-1} + ... + b_1 s + b_0}{a_n s^n + a_{n-1} s^{n-1} + ... + a_1 s + 1} \tag{2.5}$$

with $|m - n| \leq 1$ and $s = j\omega$. The concept of RFA aims to minimize the squared error between the fitting function $Z_{\text{fit}}(s)$ and the measured data $Z_{\text{meas}}(s)$ to obtain the coefficients b_i and a_i This method called Levy's technique [3]. The error is defined as:

$$e_k = Z_{\text{fit}}(s_k) - Z_{\text{meas}}(s_k) = \frac{B(s_k)}{A(s_k)} - Z_{\text{meas}}(s_k) \tag{2.6}$$

By multiplying both sides by $A(s_k)$, we obtain a new error function $\tilde{e}_k$

$$e_k A(s_k) =: \tilde{e}_k = B(s_k) - Z_{\text{meas}}(s_k) A(s_k) \tag{2.7}$$

For all frequencies from s_1 to s_ρ, where ρ is the number of frequencies. We can express (2.7) in matrix notation as

$$\tilde{\boldsymbol{e}} = \boldsymbol{M}\boldsymbol{x} - \boldsymbol{y} \tag{2.8}$$

where

$$\begin{gathered}
\tilde{\boldsymbol{e}} = \begin{bmatrix} \tilde{e}_1 \\ \vdots \\ \tilde{e}_\rho \end{bmatrix}, \quad \boldsymbol{M} = \begin{bmatrix} s_1^m & \cdots & s_1 & 1 & -Z_{\text{meas}}(s_1)s_1^n & \cdots & -Z_{\text{meas}}(s_1)s_1 \\ \vdots & & \vdots & \vdots & \vdots & & \vdots \\ s_\rho^m & \cdots & s_\rho & 1 & -Z_{\text{meas}}(s_\rho)s_\rho^n & \cdots & -Z_{\text{meas}}(s_\rho)s_\rho \end{bmatrix} \\
\boldsymbol{x} = \begin{bmatrix} b_m \\ \vdots \\ b_0 \\ a_n \\ \vdots \\ a_1 \end{bmatrix}, \quad \boldsymbol{y} = \begin{bmatrix} Z_{\text{meas}}(s_1) \\ \vdots \\ Z_{\text{meas}}(s_\rho) \end{bmatrix}
\end{gathered} \tag{2.9}$$

Due to the presence of real and imaginary components in the matrices, it is necessary to separate the real and imaginary elements. As a result, the error that requires minimization is given by:

$$\begin{bmatrix} \Re\{\tilde{\boldsymbol{e}}\} \\ \Im\{\tilde{\boldsymbol{e}}\} \end{bmatrix} = \begin{bmatrix} \Re\{\boldsymbol{M}\} \\ \Im\{\boldsymbol{M}\} \end{bmatrix} \boldsymbol{x} - \begin{bmatrix} \Re\{\boldsymbol{y}\} \\ \Im\{\boldsymbol{y}\} \end{bmatrix} \tag{2.10}$$

Therefore the cost function J that needs to be minimized is defined as:

$$\begin{aligned}
J &= \begin{bmatrix} \Re\{\tilde{\boldsymbol{e}}^T\} & \Im\{\tilde{\boldsymbol{e}}^T\} \end{bmatrix} \begin{bmatrix} \Re\{\tilde{\boldsymbol{e}}\} \\ \Im\{\tilde{\boldsymbol{e}}\} \end{bmatrix} \\
&= \left(\begin{bmatrix} \Re\{\boldsymbol{M}\} \\ \Im\{\boldsymbol{M}\} \end{bmatrix} \boldsymbol{x} - \begin{bmatrix} \Re\{\boldsymbol{y}\} \\ \Im\{\boldsymbol{y}\} \end{bmatrix} \right)^T \left(\begin{bmatrix} \Re\{\boldsymbol{M}\} \\ \Im\{\boldsymbol{M}\} \end{bmatrix} \boldsymbol{x} - \begin{bmatrix} \Re\{\boldsymbol{y}\} \\ \Im\{\boldsymbol{y}\} \end{bmatrix} \right).
\end{aligned} \tag{2.11}$$

Equation 2.11 represents a quadratic program, solvable using QR-decomposition [25]. When applied to noise-free simulated data, the RFA method demonstrates significant efficiency. However, a critical limitation arises when adapting Levy's technique to our specific application due to the well-known frequency bias problem [3]. In equation (2.5), the multiplication of $Z_{\text{meas}}(s_k)$ by $A(s_k)$ leads to rapid growth in this multiplication factor as frequency increases. Consequently, errors in the high-frequency range become more noticeable and influential than low-frequency errors. The bias introduced by $A(s_k)$ adversely impacts the accuracy of the low-frequency fit, which is undesirable, especially when accurately identifying elements such as the wire resistance of the windings of ferrite chokes. To address this issue, the RFA method has been augmented with Sanathanan-Koerner iteration [21], a technique designed to mitigate the frequency bias problem. In this iterative process, the denominator at iteration $(l-1)$, denoted as $A^{[l-1]}(s_k)$, is divided on both sides of the error defined in (2.7) for the current iteration, denoted as l.

$$\underbrace{\frac{\tilde{e}_k}{A^{[l-1]}(s_k)}}_{\tilde{e}_{\text{new},k}} = \frac{B^{[l]}(s_k)}{A^{[l-1]}(s_k)} - \frac{Z_{\text{meas}}(s_k)A^{[l]}(s_k)}{A^{[l-1]}(s_k)} \tag{2.12}$$

The bias caused by $A^{[l]}(s_k)$ is reduced by dividing it by $A^{[l-1]}(s_k)$ leading to higher fitting accuracy at Low-Frequency (LF). It can be written in matrix notation

$$\tilde{\boldsymbol{e}}_{\text{new}} = \boldsymbol{\Sigma M x} - \boldsymbol{\Sigma y} \tag{2.13}$$

Where $\boldsymbol{\Sigma}$ represents a diagonal matrix that includes the denominator of the preceding iteration $A^{[l-1]}(s_k)$ for every frequency.

$$\boldsymbol{\Sigma} = \begin{bmatrix} \frac{1}{A^{[l-1]}(s_1)} & & \\ & \ddots & \\ & & \frac{1}{A^{[l-1]}(s_\rho)} \end{bmatrix} \tag{2.14}$$

Again, separate the error function into real and imaginary component to obtain:

$$\begin{bmatrix} \Re\{\tilde{\boldsymbol{e}}_{\text{new}}\} \\ \Im\{\tilde{\boldsymbol{e}}_{\text{new}}\} \end{bmatrix} = \begin{bmatrix} \Re\{\boldsymbol{\Sigma M}\} \\ \Im\{\boldsymbol{\Sigma M}\} \end{bmatrix} \boldsymbol{x} - \begin{bmatrix} \Re\{\boldsymbol{\Sigma y}\} \\ \Im\{\boldsymbol{\Sigma y}\} \end{bmatrix} \tag{2.15}$$

When dealing with magnetic fields, the imaginary impedance component $(Z = \omega L)$ often plays a more significant role than the real component (representing losses) in the inductive domain [23]. This imbalance can have a detrimental effect on the accuracy of fitting the real component during the least squares process. To address this issue, we normalize both the real and imaginary components of equation (2.15) using weighting factors. These factors, denoted as $1/\Re(Z_{\text{fit}}^{[l-1]}(s_k))$ and $1/\Im(Z_{\text{fit}}^{[l-1]}(s_k))$, respectively, ensure that the fitting accuracy of the real and imaginary components is equivalent [23]. Therefore, the proposed IRFA formulation is utilized to extract the circuit's parameters [23].

$$\begin{bmatrix} \Re\{\tilde{\boldsymbol{e}}_{\text{new}}\} \\ \Im\{\tilde{\boldsymbol{e}}_{\text{new}}\} \end{bmatrix} = \begin{bmatrix} \Re\{\boldsymbol{W}_1\boldsymbol{\Sigma M}\} \\ \Im\{\boldsymbol{W}_2\boldsymbol{\Sigma M}\} \end{bmatrix} \boldsymbol{x} - \begin{bmatrix} \Re\{\boldsymbol{W}_1\boldsymbol{\Sigma y}\} \\ \Im\{\boldsymbol{W}_2\boldsymbol{\Sigma y}\} \end{bmatrix} \tag{2.16}$$

with the weighting $\boldsymbol{W}_1$ and $\boldsymbol{W}_2$ defined as:

$$\boldsymbol{W}_1 = \begin{bmatrix} \frac{1}{\Re\{Z_{\text{fit}}^{[l-1]}(s_1)\}} & & \\ & \ddots & \\ & & \frac{1}{\Re\{Z_{\text{fit}}^{[l-1]}(s_\rho)\}} \end{bmatrix}$$
$$\boldsymbol{W}_2 = \begin{bmatrix} \frac{1}{\Im\{Z_{\text{fit}}^{[l-1]}(s_1)\}} & & \\ & \ddots & \\ & & \frac{1}{\Im\{Z_{\text{fit}}^{[l-1]}(s_\rho)\}} \end{bmatrix} \tag{2.17}$$

The RFA method is first executed to establish a starting point. Thereafter, the IRFA method is employed until either the maximum number of iterations is reached N_{max} or the error $\varepsilon_{\text{iter}}$ is lower than the maximum error ε_{max}

$$\varepsilon_{\text{iter}} = \max_k \frac{|Z_{\text{fit}}(s_k) - Z_{\text{meas}}(s_k)|}{|Z_{\text{meas}}(s_k)|}.$$

And at each iteration, we ensure that the poles are stable $\Re\{p_i\} < 0$ (See Appendix A) by reflecting the real positive pole onto the negative side.

$$\Re\{p_i\} = -\Re\{p_i\}.$$

The subsequent step is to derive the residue and poles of the fitting curve $Z_{\text{fit}}(s)$ represented as

$$Z_{\text{fit}}(s) = d + e\,s + \sum_{i=1}^{n} \frac{k_i}{s - p_i} \tag{2.18}$$

Note that k_i and p_i can be complex number.

$$Z(s) = d + e\,s + \underbrace{\sum_{i=1}^{N_r} \frac{r_i}{s - p_i}}_{\text{real pole}} + \underbrace{\sum_{i=1}^{N_c} \frac{a_i s + b_i}{s^2 + m_i s + n_i}}_{\text{complex conjugate pole pairs}} \tag{2.19}$$

where N_r is the number of real poles and N_c is the number of the complex conjugate poles pairs. Note that the variables a_i, b_i, m_i, and n_i used in this context differ from those used in equation (2.5). The function $Z(s)$ can be expressed as the sum of a constant term d, a term proportional to s denoted e, and terms for the residue of real poles and residue pairs of complex conjugate poles. The same equation applies when expressing the admittance $Y(s)$. Here, the constant d corresponds to either electric resistance for $Z(s)$ or electric conductance for $Y(s)$. Meanwhile, $e\,s$ corresponds to electric capacitance for $Y(s)$ or inductance for $Z(s)$. Table 2.1 and 2.2 provide details for synthesizing real-pole and complex-pole pair terms.

- ***Real Pole***: When conducting circuit analysis, positive residue values (r_i) lead to a simplified equivalent circuit in either a series RL configuration for admittance or a parallel RC configuration for impedance, as Table 2.1 and 2.2 indicates. However, negative residue values present challenges via the

IRFA, resulting in the appearance of negative values of circuit elements. In practical circuit design, negative elements are typically unwanted and should be avoided. However, negative elements can be utilized to create a more precise equivalent circuit in the context of EMI modeling and simulation in the frequency domain. Nevertheless, the management of negative elements in time-domain simulations can present challenges. To tackle this challenge, [23] suggests an inventive solution: pairing a positively valued cell with a negative resistor, as demonstrated in Table 2.1 and 2.2. For instance, when encountering a negative residue r_i originating from a stable real pole $p_i < 0$ in the admittance representation $Y(s)$, this commonly results in a negative RL series configuration. However, Table 2.1 and 2.2 shows that a circuit combining a positive RC series cell in parallel with a negative resistance $-R$ can be utilized. This particular circuit is equivalent in functionality to the negative RL series circuit due to its shared rational function. The negative resistance $-R$ is then integrated into Equation (2.19) as the constant term d, which results in a modified constant term $d^* = d - \frac{1}{R} = d - \frac{r_i}{p_i}$. A comparable analysis can be applied to impedance $Z(s)$. These circuits can minimize negative elements resulting from real pole terms.

- ***Complex-pole pair***: A practical approach when dealing with complex pole-pairs involves the utilization of a four-element circuit. This method represents the minimal realization, involving four independent variables: a_i, b_i, m_i, and n_i in the rational function (See Table 2.1 and 2.2). Alternatively, an "extended" circuit type, comprising six elements but offering more straightforward parameter calculation formulas, can be employed [23]. Since both m_i and n_i are positive, resulting from the stable poles ($\Re\{p_i\} < 0$), the coefficients a_i and b_i may take negative values. Thus, the value of the lumped element is negative, and a passivity test is required to ensure the system does not produce or amplify energy.

Term		$Y(s)$	
		Circuit	Expression
Real pole $\frac{r_i}{s-p_i}$	$r_i > 0$	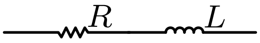	$L = 1/r_i$ $R = -p_i/r_i$
	$r_i < 0$	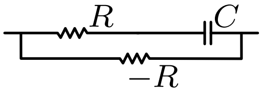	$R = p_i/r_i$ $C = -1/(p_i R)$
Complex pole Pair $\frac{a_i s+b_i}{s^2+m_i s+n_i}$	*Minimal Type*	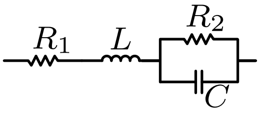	$L = 1/a_i$ $R_1 = Lm_i - Lb_i$ $R_2 = n_i/b_i - R_1$ $C = 1/(b_i L R_2)$
	Extended Type	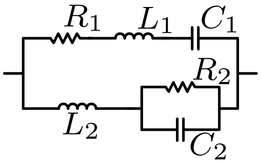	$R_1 = n_i/b_i$ $C_1 = 1/(m_i R_1)$ $L_1 = 1/(n_i C_1)$ $L_2 = (a_i - 1/L_1)^{-1}$ $R_2 = m_i L_2$ $C_2 = 1/(n_i L_2)$

Table 2.1: *Equivalent circuit synthesis for the admittance [23].*

Term		$Z(s)$	
		Circuit	Expression
Real pole $\frac{r_i}{s-p_i}$	$r_i > 0$	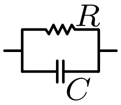	$C = 1/r_i$ $R = -r_i/p_i$
	$r_i < 0$	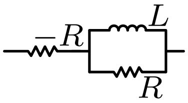	$R = r_i/p_i$ $L = -R/p_i$
Complex pole Pair $\frac{a_i s+b_i}{s^2+m_i s+n_i}$	*Minimal Type*	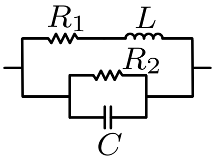	$C = 1/a_i$ $R_2 = (Cm_i - C^2 b_i)^{-1}$ $R_1 = (n_i/b_i - 1/R_2)^{-1}$ $L = R_1/(b_i C)$
	Extended Type	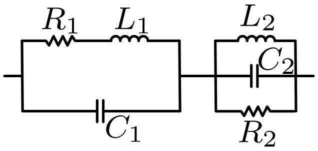	$R_1 = b_i/n_i$ $L_1 = R_1/m_i$ $C_1 = 1/(n_i L_1)$ $C_2 = (a_i - 1/C_1)^{-1}$ $R_2 = 1/(m_i C_2)$ $L_2 = 1/(n_i C_2)$

Table 2.2: *Equivalent circuit synthesis for the impedance [23].*

CHAPTER

3

Darwin approximation

In this chapter, the Finite-Element (FE) of the Darwin approximation is discussed and its well-known derivation is presented for the sake of completeness and consistency

3.1 Introduction

The original intent of the Darwin model was to illustrate the electromagnetic field produced by moving charges in free space while disregarding wave propagation [11]. The model decomposes the electric field $\boldsymbol{E}$ into two components: the transverse component $\boldsymbol{E}_\mathrm{T}$ and the longitudinal component $\boldsymbol{E}_\mathrm{L}$ [11]. However, in more recent usage, the Darwin model has been employed to characterize the electro-magneto-quasistatic field, taking into account nonhomogeneous materials rather than just free space. Consequently, it becomes possible to explore the behavior of capacitive, inductive, and resistive elements when the magnetic energy density w_m is not significantly different from the electric energy density w_e. One notable challenge with the Darwin model is that its solution is not inherently unique without the introduction of an implicit or explicit gauge. An example of a gauge is the Coulomb type gauge, expressed as $j\omega\nabla\cdot(\varepsilon\boldsymbol{A}) = 0$. By discretizing using the Coulomb gauge, the resulting system matrix is symmetric, but the number of iterations increases at high frequencies. Consequently, efforts have been made to introduce redundant variables χ to improve the convergence properties of the iterative solver [12].

$$\boldsymbol{A} = \boldsymbol{A}' + \frac{1}{j\omega}\nabla\chi, \qquad \varphi = \varphi' - \chi$$

In the following, the most important results from [6] regarding the two-step Darwin approximation is examined and recapitulated. Initially, the electro-quasistatic field problem is solved independently of the magnetic vector potential in the first step. The resulting solenoidal total current densities are then used as an excitation source for a magneto-quasistatic (MQS) curl-curl formulation based on the magnetic vector potential. The resulting equation involves the regularization of the magneto-quasistatic continuity equation, particularly in the conductive regions (Ω_c) within the problem domain. However, the combination of the Darwin-Ampère equation and the electro-quasistatic continuity gauge imposes limitations on the modeling capabilities. The formulation is unable to capture inductively driven displacements of space charges at the interface between conductive (Ω_c) and non-conductive (Ω_n) regions, which serve as sources for electro-quasistatic field contributions in the non-conductive regions. The lack of continuity of normal components of total current densities at conductor/non-conductor interfaces is a constraint of the two-step scheme. An attempt to address this limitation involves the introduction of an artificial conductivity value ($\hat{\gamma}$) in non-conductive regions, resulting in regularization but introducing phase errors in the calculated electric field approximations. In [20], research explored that characterizing the scalar potential at the electric port using Poynting's theorem can be viewed as a physical voltage excitation, but only up to frequencies where the Darwin model's validity is compromised. This holds true solely when the electric ports is located at the outer boundary. The Darwin approximation simplifies Maxwell's equations by excluding wave propagation effects. It provides insights into resistive, inductive, and capacitive behaviors in contrast to electro-quasi-static (which deals only with resistive and capacitive characteristics) and magneto-quasi-static (referred to as the eddy current problem, which considers only resistive and inductive characteristics). The Darwin approximation is suitable when wave propagation is not dominant [14]. To meet the requirements for the Darwin approximation, the frequency f must satisfy the condition:

$$f \ll f_{\max} = \frac{c_{\min}}{d} = \frac{c_0}{d\sqrt{\mu_{\mathrm{r,max}} \cdot \varepsilon_{\mathrm{r,max}}}}, \tag{3.1}$$

Here, the spatial domain is represented by d, c_0 represents the speed of light in vacuum, while the maximum relative permeability and maximum relative permittivity are denoted by $\mu_{\mathrm{r,max}}$ and $\varepsilon_{\mathrm{r,max}}$, respectively.

3.2 Maxwell's Equation

The complete set of Maxwell's equations in the frequency domain can be written as follows:

$$\nabla \times \hat{\boldsymbol{H}} = \hat{\boldsymbol{J}} + j\omega\hat{\boldsymbol{D}}, \qquad (\textit{Ampere's law}) \tag{3.2}$$

$$\nabla \times \hat{\boldsymbol{E}} = -j\omega\hat{\boldsymbol{B}}, \qquad (\textit{Farady's law}) \tag{3.3}$$

$$\nabla \cdot \hat{\boldsymbol{D}} = \rho, \qquad (\textit{Gauss's law}) \tag{3.4}$$

$$\nabla \cdot \hat{\boldsymbol{B}} = 0, \qquad (\textit{no magnetic monopoles}) \tag{3.5}$$

The charge density (ρ) and the current density ($\hat{\boldsymbol{J}}$) are related by the continuity equation:

$$\nabla \cdot \hat{\boldsymbol{J}} = -j\omega\rho. \tag{3.6}$$

Table 3.1 provides information on electromagnetic field quantities and their units, with the subscript $(\hat{\cdot})$ denoting a complex vector field.

Notation	Units	Description
$\hat{\boldsymbol{H}}$	A/m	Magnetic field intensity
$\hat{\boldsymbol{J}}$	A/m^2	Current density
$\hat{\boldsymbol{D}}$	As/m^2	Electric flux density
$\hat{\boldsymbol{E}}$	V/m	Electric field intensity
$\hat{\boldsymbol{B}}$	Vs/m	Magnetic flux density
ρ	As/m^3	Charge density

Table 3.1: Electromagnetic field quantities.

In addition, the following constitutive equations couple the electromagnetic fields:

$$\hat{\boldsymbol{B}} = \mu \hat{\boldsymbol{H}} \tag{3.7}$$

$$\hat{\boldsymbol{D}} = \varepsilon \hat{\boldsymbol{E}} \tag{3.8}$$

$$\hat{\boldsymbol{J}} = \hat{\boldsymbol{J}}_\mathrm{s} + \gamma \hat{\boldsymbol{E}} \tag{3.9}$$

Where μ, ε and γ denote magnetic permeability in (Vs/Am), electric permittivity in (As/Vm) and electric conductivity in (A/Vm) respectively.

3.3 Electric Field Decomposition

The Darwin approximation decomposes the electric field intensity $\hat{\boldsymbol{E}}$ into two parts: the transverse component $\hat{\boldsymbol{E}}_\mathrm{T}$ and the longitudinal component $\hat{\boldsymbol{E}}_\mathrm{L}$ [11].

$$\hat{\boldsymbol{E}} = \hat{\boldsymbol{E}}_\mathrm{T} + \hat{\boldsymbol{E}}_\mathrm{L}. \tag{3.10}$$

The transverse component acts as the divergence-free source.

$$\nabla \cdot \hat{\boldsymbol{E}}_\mathrm{T} = 0, \tag{3.11}$$

Conversely, the longitudinal component acts as a curl-free source.

$$\nabla \times \hat{\boldsymbol{E}}_\mathrm{L} = \mathbf{0}. \tag{3.12}$$

3.4 Magnetic Vector Potential

Equation (3.5) expresses the magnetic field density as the curl of a vector field:

$$\hat{\boldsymbol{B}} = \nabla \times \hat{\boldsymbol{A}}. \tag{3.13}$$

where $\hat{\boldsymbol{A}}$ is known as the magnetic vector potential. By utilizing equations (3.10), (3.12), and (3.13) within Faraday's law (3.3), we arrive at the following relationship:

$$\nabla \times \hat{\boldsymbol{E}}_\mathrm{T} = -j\omega \nabla \times \hat{\boldsymbol{A}} \tag{3.14}$$

$$\hat{\boldsymbol{E}}_\mathrm{T} = -j\omega \hat{\boldsymbol{A}}. \tag{3.15}$$

3.5 Electric Scalar Potential

A curl free source of a vector field (3.12) can be represented as a gradient of a scalar potential:

$$\nabla \times \hat{\boldsymbol{E}}_{\mathrm{L}} = \boldsymbol{0} \Rightarrow \hat{\boldsymbol{E}}_{\mathrm{L}} = -\nabla \hat{\varphi}, \tag{3.16}$$

$\hat{\varphi}$ denotes to the electric scalar potential.

3.6 Derivation of Darwin PDE

Using the equations (3.15) and (3.16) the electric field value can be obtained. Inserting these equations into (3.8) and (3.16) in the context of (3.4), we get the following equation

$$\nabla \cdot \varepsilon \hat{\boldsymbol{E}}_{\mathrm{L}} = \rho \Rightarrow \nabla \cdot \varepsilon \nabla \hat{\varphi} = -\rho \tag{3.17}$$

Additionally, we substitute (3.7), (3.8), (3.9) and (3.10) in the Ampere's law (3.2) to achieve the first Partial Differential Equation (PDE) of the Darwin approximation. The first PDE of the Darwin approximation can be obtained by replacing the constitutive equations (3.7), (3.8), (3.9), and (3.10) in Ampere's law (3.2).

$$\nabla \times \underbrace{\nu \nabla \times \hat{\boldsymbol{A}}}_{\hat{\boldsymbol{H}}} = \hat{\boldsymbol{J}}_{\mathrm{s}} \underbrace{-\gamma \nabla \hat{\varphi} - j\omega\gamma \hat{\boldsymbol{A}}}_{\gamma \hat{\boldsymbol{E}}} \underbrace{-j\omega\varepsilon \nabla \hat{\varphi} + \omega^2 \varepsilon \hat{\boldsymbol{A}}}_{j\omega \hat{\boldsymbol{D}}} \tag{3.18}$$

In Darwin approximation the propagation component is neglected, i.e., $\omega^2 \hat{\boldsymbol{A}}$ is neglected.

$$\nabla \times \nu \nabla \times \hat{\boldsymbol{A}} + \gamma \nabla \hat{\varphi} + j\omega\gamma \hat{\boldsymbol{A}} + j\omega\varepsilon \nabla \hat{\varphi} = \hat{\boldsymbol{J}}_{\mathrm{s}} \tag{3.19}$$

Applying the divergence to (3.19) grants the continuity equation (3.6) and expressed as:

$$\nabla \cdot \gamma \hat{\varphi} + j\omega \nabla \cdot \gamma \hat{\boldsymbol{A}} + j\omega \nabla \cdot \varepsilon \nabla \hat{\varphi} = \nabla \cdot \hat{\boldsymbol{J}}_{\mathrm{s}} \tag{3.20}$$

Note that any solution pair $(\hat{\boldsymbol{A}}, \hat{\varphi})$ that satisfies equation (3.19) also satisfies equation (3.20). Consequently, an additional equation is needed to ensure that the pair $(\hat{\boldsymbol{A}}, \hat{\varphi})$ is unique. To solve this ill-posedness problem, we introduce a Coulomb gauge as follows [26]:

$$j\omega \nabla \cdot \varepsilon \hat{\boldsymbol{A}} = 0 \tag{3.21}$$

Furthermore, in [26], it is proposed to introduce a Lagrange multiplier denoted as p to ensure the symmetry of the system matrix. Consequently, the Darwin PDE can be expressed as follows:

$$\nabla \times \nu \nabla \times \hat{\boldsymbol{A}} + \gamma \nabla \hat{\varphi} + j\omega\gamma \hat{\boldsymbol{A}} + j\omega\varepsilon \nabla \hat{\varphi} - j\omega\varepsilon \nabla p = \hat{\boldsymbol{J}}_{\mathrm{s}} \tag{3.22}$$

$$\frac{1}{j\omega} \nabla \cdot (-j\omega\gamma \hat{\boldsymbol{A}} - \gamma \nabla \hat{\varphi} - j\omega\varepsilon \nabla \hat{\varphi}) - j\omega \nabla \cdot \varepsilon \hat{\boldsymbol{A}} = 0 \tag{3.23}$$

$$-j\omega \nabla \cdot \varepsilon \hat{\boldsymbol{A}} = 0 \tag{3.24}$$

3.7 Finite Element Method

The FEM is a numerical technique for solving engineering and mathematical modeling differential equations. It is utilized for approximating solutions to problems in various fields like structural analysis, heat transfer, fluid flow, mass transport, and electromagnetic problems [13].

To apply FEM, the first step, as presented in, e.g., [13], is to transform the differential equations, such as those represented by the equations (3.22), (3.23), and (3.24), from their strong form to a weak form. Let us start with (3.22). This strong to weak transformation is done by multiplying the equation by a test function $\boldsymbol{W}$ (in this case, a dot product) and then integrating over the entire domain. This process yields

$$\int_\Omega \boldsymbol{W} \cdot (\nabla \times \nu \nabla \times \hat{\boldsymbol{A}} + \gamma \nabla \hat{\varphi} + j\omega\gamma \hat{\boldsymbol{A}} + j\omega\varepsilon \nabla \hat{\varphi} - j\omega\varepsilon \nabla p)\, d\Omega = \int_\Omega \boldsymbol{W} \cdot \hat{\boldsymbol{J}}_\mathrm{s}\, d\Omega \tag{3.25}$$

The first term can be expressed as:

$$\boldsymbol{W} \cdot (\nabla \times \nu \nabla \times \hat{\boldsymbol{A}}) = -\nabla \cdot (\boldsymbol{W} \times \nu \nabla \times \hat{\boldsymbol{A}}) + (\nabla \times \boldsymbol{W}) \cdot (\nu \nabla \times \hat{\boldsymbol{A}}) \tag{3.26}$$

Substituting this into (3.25), we obtain:

$$\begin{aligned} &- \int_\Omega \nabla \cdot (\boldsymbol{W} \times \nu \nabla \times \hat{\boldsymbol{A}})\, d\Omega + \int_\Omega (\nabla \times \boldsymbol{W}) \cdot (\nu \nabla \times \hat{\boldsymbol{A}})\, d\Omega \\ &+ \int_\Omega \gamma \boldsymbol{W} \cdot \nabla \hat{\varphi}\, d\Omega + \int_\Omega j\omega\gamma \boldsymbol{W} \cdot \hat{\boldsymbol{A}}\, d\Omega + \int_\Omega j\omega\varepsilon \boldsymbol{W} \cdot \nabla \hat{\varphi}\, d\Omega - \int_\Omega j\omega\varepsilon \boldsymbol{W} \cdot \nabla p\, d\Omega \\ &= \int_\Omega \boldsymbol{W} \cdot \boldsymbol{J}_s\, d\Omega \end{aligned} \tag{3.27}$$

Using Gauss's theorem, the first integral term can be written as a closed surface integral. Therefore, it can be expressed as:

$$\int_\Omega \nabla \cdot (\boldsymbol{W} \times \nu \nabla \times \hat{\boldsymbol{A}})\, d\Omega = \oint_{\partial\Omega} \boldsymbol{n} \cdot (\boldsymbol{W} \times \nu \nabla \times \hat{\boldsymbol{A}})\, d\Gamma = \oint_{\partial\Omega} \boldsymbol{W} \cdot (\boldsymbol{n} \times \nu \nabla \times \hat{\boldsymbol{A}})\, d\Gamma \tag{3.28}$$

For our problem, the term $\nu \nabla \times \boldsymbol{n} \times \boldsymbol{A}$ equals zero. This implies a homogeneous Neumann boundary at $\partial\Omega$, meaning there is no current surface at the boundary. Therefore, the first equation of the weak form can be expressed as follows:

$$\begin{aligned} &\int_\Omega (\nabla \times \boldsymbol{W}) \cdot (\nu \nabla \times \hat{\boldsymbol{A}})\, d\Omega + \int_\Omega \gamma \boldsymbol{W} \cdot \nabla \hat{\varphi}\, d\Omega + \int_\Omega j\omega\gamma \boldsymbol{W} \cdot \hat{\boldsymbol{A}}\, d\Omega \\ &+ \int_\Omega j\omega\varepsilon \boldsymbol{W} \cdot \nabla \hat{\varphi}\, d\Omega - \int_\Omega j\omega\varepsilon \boldsymbol{W} \cdot \nabla p\, d\Omega = \int_\Omega \boldsymbol{W} \cdot \boldsymbol{J}_\mathrm{s}\, d\Omega \end{aligned} \tag{3.29}$$

The second PDE in the equation (3.23) is multiplied by a scalar test function u and integrated over the entire domain Ω.

$$-\int_\Omega u \nabla \cdot \gamma \hat{\boldsymbol{A}} + u \frac{1}{j\omega} \nabla \cdot \gamma \nabla \hat{\varphi} + u \nabla \cdot \varepsilon \nabla \hat{\varphi} + j\omega u \nabla \cdot \varepsilon \hat{\boldsymbol{A}}\, d\Omega = 0. \tag{3.30}$$

Again, the product rule is applied to the second and third terms of the equation (3.30) as well as the Gauss's theorem.

$$\nabla \cdot (a\boldsymbol{W}) = a \nabla \cdot \boldsymbol{W} + (\nabla a) \cdot \boldsymbol{W} \Rightarrow a \nabla \cdot \boldsymbol{W} = \nabla \cdot (a\boldsymbol{W}) - (\nabla a) \cdot \boldsymbol{W} \tag{3.31}$$

$$\begin{aligned}\int_\Omega u\nabla\cdot(\gamma+j\omega\varepsilon)\nabla\hat{\varphi} &= \\ &\oint_{\partial\Omega} u(\gamma+j\omega\varepsilon)\nabla\hat{\varphi}\cdot\boldsymbol{n}\,d\,\Gamma - \int_\Omega \nabla u\cdot(\gamma+j\omega\varepsilon)\nabla\hat{\varphi}\,d\,\Omega\end{aligned} \tag{3.32}$$

The term $\nabla\hat{\varphi}\cdot\boldsymbol{n}$ describes the Neumann boundary condition. In this problem, a homogeneous Neumann boundary is defined at the boundary of the scalar potential.

$$\begin{aligned}&-\int_\Omega u\nabla\cdot\gamma\hat{\boldsymbol{A}}\,d\Omega + \frac{1}{j\omega}\int_\Omega \nabla u\cdot\gamma\nabla\hat{\varphi}\,d\Omega + \\ &+\int_\Omega \nabla u\cdot\varepsilon\nabla\hat{\varphi}\,d\Omega - j\omega\int_\Omega u\nabla\cdot\hat{\boldsymbol{A}}\,d\Omega = 0\end{aligned} \tag{3.33}$$

Moreover, we multiply the last PDE with another test function v.

$$-j\omega\int_\Omega v\nabla\cdot\varepsilon\hat{\boldsymbol{A}}\,d\Omega = 0. \tag{3.34}$$

3.7.1 Discretization

To obtain the system matrices required for solving the weak form, we implement a discretization method for the test functions ($\boldsymbol{W}$,u,v) and for the unknown parameters ($\hat{\boldsymbol{A}}$,$\hat{\varphi}$,p). Specifically, during this discretization process, we use edge elements to represent the magnetic vector potential $\hat{\boldsymbol{A}}$ and the test function $\boldsymbol{W}$, while the scalar electric potential $\hat{\varphi}$ and the Lagrange multiplier p are discretized as nodal elements.

$$\hat{\boldsymbol{A}} \approx \sum_{i=1}^{n_{eq}} \boldsymbol{N}_i\hat{A}_i, \qquad \boldsymbol{W} \approx \sum_{i=1}^{n_{eq}} \boldsymbol{N}_i W_i \tag{3.35}$$

$$\hat{\varphi} \approx \sum_{i=1}^{n_{eq}} N_i\hat{\varphi}_i, \qquad u \approx \sum_{i=1}^{n_{eq}} N_i u_i \tag{3.36}$$

$$p \approx \sum_{i=1}^{n_{eq}} N_i p_i, \qquad v \approx \sum_{i=1}^{n_{eq}} N_i v_i \tag{3.37}$$

where $\boldsymbol{N}_i$ and N_i represent the shape functions associated with the i-th edge and node, respectively. We apply these approximations to the equations (3.29), (3.32), and (3.34), resulting in the following equation in matrix form.

$$\begin{aligned}\sum_{i=1}^{n_{eq}}\sum_{j=1}^{n_{eq}} W_i \Bigg(&\int_\Omega (\nabla\times\boldsymbol{N}_i)\cdot(\nu\nabla\times\boldsymbol{N}_j)\hat{A}_j\,d\Omega + \int_\Omega \gamma\boldsymbol{N}_i\cdot\nabla N_j\hat{\varphi}_j\,d\Omega \\ &+\int_\Omega j\omega\gamma\boldsymbol{N}_i\cdot\boldsymbol{N}_j A_j\,d\Omega + \int_\Omega j\omega\varepsilon\boldsymbol{N}_i\cdot\nabla N_j\hat{\varphi}_j\,d\Omega \\ &-\int_\Omega j\omega\varepsilon\boldsymbol{N}_i\cdot\nabla N_j p_j\,d\Omega - \int_\Omega \boldsymbol{N}_i\cdot\boldsymbol{J}_\mathrm{s}\,d\Omega\Bigg) = 0\end{aligned} \tag{3.38}$$

$$\begin{aligned}\sum_{i=1}^{n_{eq}}\sum_{j=1}^{n_{eq}} u_i \Bigg(&-\int_\Omega N_i\nabla\cdot\gamma\boldsymbol{N}_j\hat{A}_j\,d\Omega + \frac{1}{j\omega}\int_\Omega \nabla N_i\cdot\gamma\nabla N_j\hat{\varphi}_j\,d\Omega \\ &+\int_\Omega \nabla N_i\cdot\varepsilon\nabla N_j\hat{\varphi}_j\,d\Omega - j\omega\int_\Omega N_i\nabla\cdot\boldsymbol{N}_j\hat{A}_j\,d\Omega\Bigg) = 0\end{aligned} \tag{3.39}$$

$$\sum_{i=1}^{n_{eq}}\sum_{j=1}^{n_{eq}} -v_i j\omega \int_{\Omega} N_i \nabla \cdot \varepsilon \boldsymbol{N}_j \hat{A}_j \, d\Omega = 0. \tag{3.40}$$

The sum of (3.38), (3.39) and (3.40) need to be fulfilled independent on the test function W_i, u_i and v_i. Therefore we can write it in the matrix form

$$\boldsymbol{M}\boldsymbol{x} = \boldsymbol{b} \tag{3.41}$$

Where

$$\boldsymbol{M} = \begin{bmatrix} \boldsymbol{M}_{\boldsymbol{AA},\nu} + j\omega \boldsymbol{K}_{\boldsymbol{AA},\gamma} & \boldsymbol{M}_{\boldsymbol{A}\varphi,\gamma} + j\omega \boldsymbol{K}_{\boldsymbol{A}\varphi,\varepsilon} & -j\omega \boldsymbol{K}_{\boldsymbol{A}p,\varepsilon} \\ \boldsymbol{M}_{\varphi\boldsymbol{A},\gamma} + j\omega \boldsymbol{K}_{\varphi\boldsymbol{A},\varepsilon} & \frac{1}{j\omega}\boldsymbol{K}_{\varphi\varphi,\gamma} + \boldsymbol{K}_{\varphi\varphi,\varepsilon} & \boldsymbol{0} \\ -j\omega \boldsymbol{K}_{p\boldsymbol{A},\varepsilon} & \boldsymbol{0} & \boldsymbol{0} \end{bmatrix} \tag{3.42}$$

$$\boldsymbol{x} = [\boldsymbol{A}_j, \quad \hat{\varphi}, \quad \hat{p}]^T, \qquad \boldsymbol{b} = [\boldsymbol{J}, \quad 0, \quad 0]^T \tag{3.43}$$

where

$$\boldsymbol{K}_{\boldsymbol{AA},\nu} = \int (\nabla \times \boldsymbol{N}_i) \cdot (\nu \nabla \times \boldsymbol{N}_j) \, d\Omega \qquad \boldsymbol{K}_{\boldsymbol{AA},\gamma} = \int \gamma \boldsymbol{N}_i \cdot \boldsymbol{N}_j \, d\Omega$$

$$\boldsymbol{K}_{\boldsymbol{A}\varphi,\gamma} = \int \gamma \boldsymbol{N}_i \cdot \nabla N_j \, d\Omega \qquad \boldsymbol{K}_{\boldsymbol{A}\boldsymbol{\varphi},\varepsilon} = \int \varepsilon \boldsymbol{N}_i \cdot \nabla N_j \, d\Omega$$

$$\boldsymbol{K}_{\boldsymbol{\varphi\varphi},\gamma} = \int \gamma \nabla N_i \cdot \nabla N_j \, d\Omega \qquad \boldsymbol{K}_{\boldsymbol{\varphi\varphi},\varepsilon} = \int \varepsilon \nabla N_i \cdot \nabla N_j \, d\Omega$$

$$\boldsymbol{K}_{\boldsymbol{A}p,\varepsilon} = \int \varepsilon \boldsymbol{N}_i \cdot \nabla N_j \, d\Omega \qquad \boldsymbol{J}_i = \int \boldsymbol{N}_i \cdot \boldsymbol{J}_{\mathrm{s}} \, d\Omega$$

The matrices $\boldsymbol{K}_{\varphi\boldsymbol{A},\gamma}$, $\boldsymbol{K}_{\varphi\boldsymbol{A},\varepsilon}$ and $\boldsymbol{K}_{p\boldsymbol{A},\varepsilon}$ are the transpose of $\boldsymbol{K}_{\boldsymbol{A}\varphi,\gamma}$, $\boldsymbol{K}_{\boldsymbol{A}\varphi,\varepsilon}$ and $\boldsymbol{K}_{\boldsymbol{A}p,\varepsilon}$, respectively.

CHAPTER 4

Choke Modeling

In this chapter, we will explore the geometry of the choke to be simulated, along with a comprehensive examination of the complex permeability characteristics of the ferrite choke.

4.1 Choke Model

Figure 4.1 demonstrates the choke used for simulation purposes, constructed using an E-Core-shaped ferrite. This choke consists of two copper wires, each of which is inserted into one of the holes in the ferrite. The copper wires have dimensions of 100 mm in length, 2 mm in height, and 5 mm in width. The dimensions of the ferrite itself dimensions are illustrated in Figure 4.1.

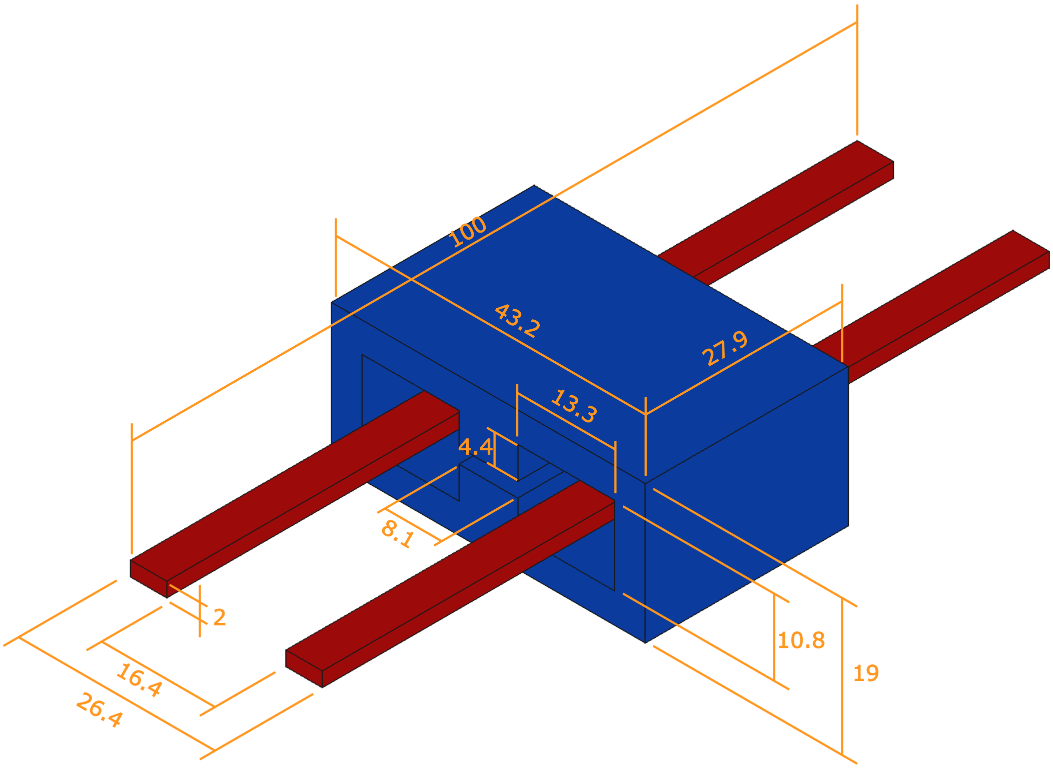

Figure 4.1: Ferrite Choke (all dimension in mm).

4.2 Ferrite Permeability

The complex permeability characteristics of the ferrite choke were analyzed for three different materials. Two of these materials were from Fair-Rite [1], while the third was from TDK [2].

4.2.1 Fair-rite 75

The first ferrite is Fair-Rite 75 material. The properties of Fair-Rite 75 is shown on Table 4.1. The complex permeability's behavior has two distinct curves in Figure 4.2. The blue curve (μ') represents the real component and the orange curve (μ'') represents the imaginary component. The real component dominates at frequencies below 100 kHz, leading to an impedance similar to that of an inductor. As frequencies rise above 100 kHz, the imaginary component becomes predominant and causes increasing losses that peak around 1.5 MHz, followed by a gradual decrease.

Property	*Symbol*	*Unit*	*Value*
Initial Permeability	μ_i		5000
Flux Density @ Field Strength	B H	mT A/m	480 398
Residual Flux Density	B_r	mT	100
Coercive Force	H_c	A/m	9
Conductivity	γ	S/m	0.3333

Table 4.1: Material properties of Fair-rite 75.

4.2.2 Fair-rite 98

The second ferrite used is made of Fair-Rite 98 material, whose properties are displayed in detail in Table 4.2. Although its behavior is similar to that of Fair-Rite 75, the imaginary component of Fair-Rite 98 changes more rapidly. Compared to Fair-Rite 75, this ferrite exhibits lower initial permeability. Its complex permeability is illustrated in Figure 4.3. Note that the imaginary component's peak exceeds the initial permeability value.

Property	*Symbol*	*Unit*	*Value*
Initial Permeability	μ_i		2400
Flux Density @ Field Strength	B H	mT A/m	500 398
Residual Flux Density	B_r	mT	200
Coercive Force	H_c	A/m	14
Conductivity	γ	S/m	0.5

Table 4.2: Material properties of Fair-rite 98.

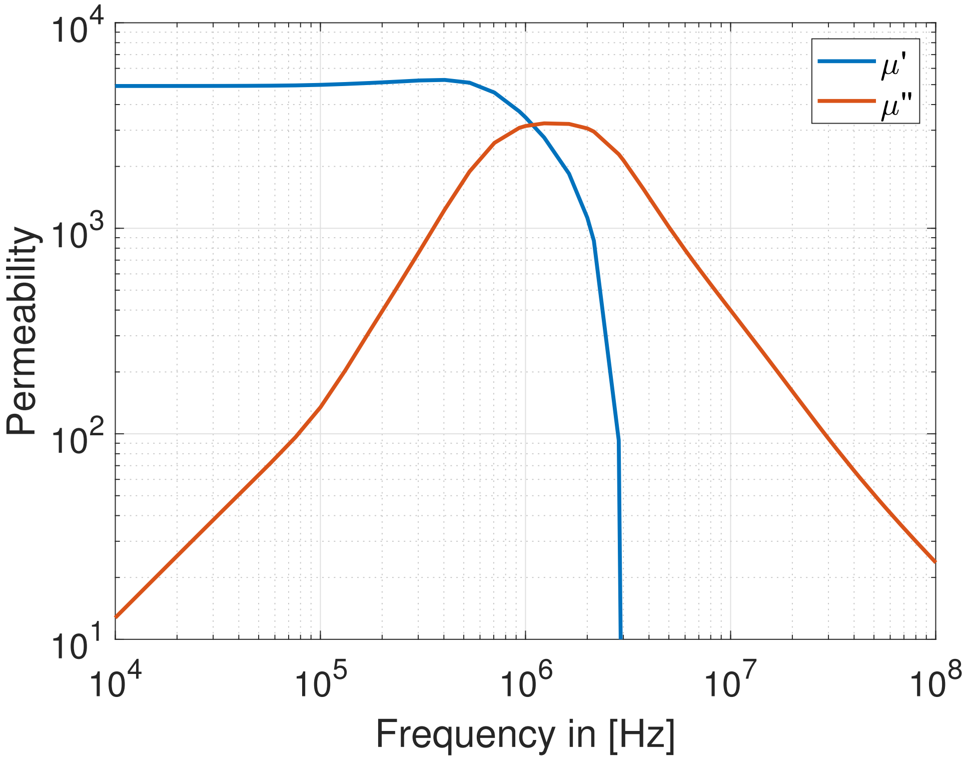

Figure 4.2: Complex permeability of Fair-rite 75 material.

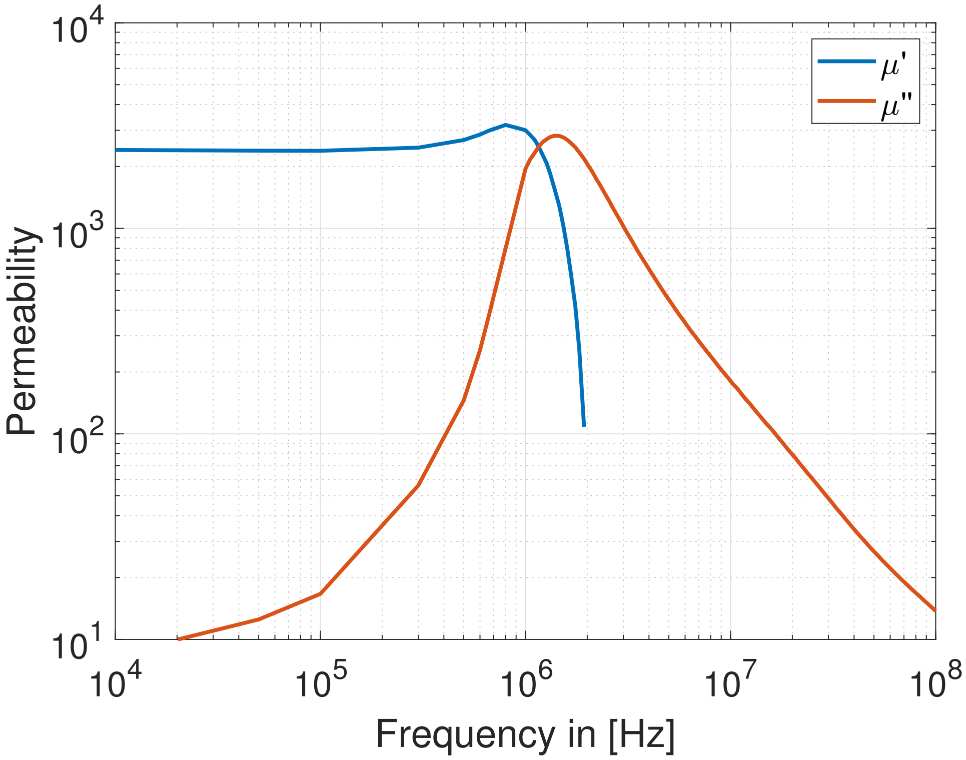

Figure 4.3: Complex permeability of Fair-rite 98 material.

4.2.3 TDK T37

The final ferrite material used is TDK T37. The properties of TDK T37 are presented in Table 4.3, while the complex permeability is depicted in Figure 4.4. In comparison to 75 and 98, TDK T37 exhibits relatively low loss. Unlike Fair-rite 75 and 98, the real component of TDK T37 does not decrease quickly.

Property	*Symbol*	*Unit*	*Value*
Initial Permeability	μ_i		6500
Meas. field strength	H	A/m	1200
Flux density	B	mT	380
Optimum	f_{min}	MHz	0.01
frequency range	f_{max}	MHz	0.30
Coercive Force	H_c	A/m	9
Conductivity	γ	S/m	5

Table 4.3: Material properties of TDK T37.

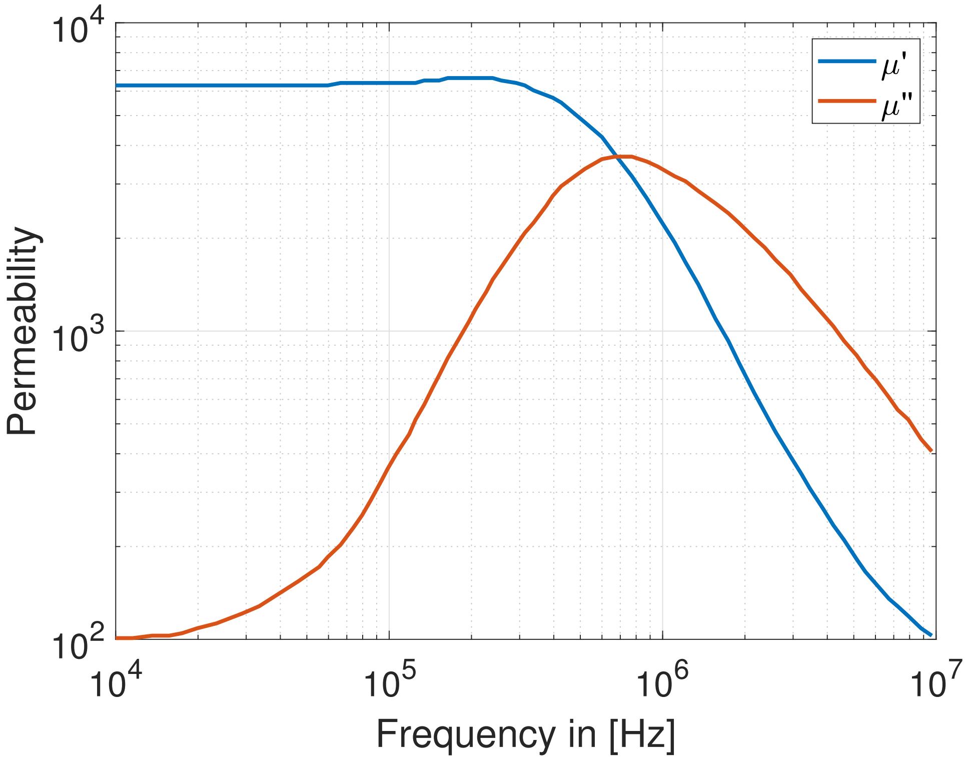

Figure 4.4: Complex permeability of TDK T37 material.

CHAPTER

5

Simulation and Results

This chapter investigates the utilization of software to simulate the behavior of a ferrite choke. The Darwin approximation is realized through the application of openCFS, while the full-wave Maxwell's equations are solved by CST, providing a reference to the Darwin approximation. It is important to point out that the Darwin approach is suitable for frequencies where wave effects are not dominant. Furthermore, an examination of the particular configurations employed in each software, encompassing boundary conditions and excitation, will be conducted.

5.1 openCFS

Coupled Field Simulation (openCFS) is a finite element-based multi-physics modeling and simulation tool [8]. The Darwin approximation derived in Chapter 3 is implemented in openCFS (using Direct solver). Figure 5.1 shows the boundaries of the ferrite choke. The choke model is excited with voltages using a Dirichlet boundary at the boundary of the wire. Therefore in CM, the following boundary conditions are applied:

- At Γ_1 and Γ_2, the electric scalar potential $\hat{\varphi}$ has inhomogeneous Dirichlet boundary conditions with an amplitude of 1 V, while the Lagrange multiplier p has homogeneous Dirichlet boundary conditions. Additionally, a homogeneous Neumann boundary condition is utilized for the magnetic vector potential $\hat{\boldsymbol{A}}$ (i.e. $\hat{\boldsymbol{B}} \cdot \boldsymbol{n} = 0$).

- At Γ_3 and Γ_4, the electric scalar potential $\hat{\varphi}$ has inhomogeneous Dirichlet boundary conditions with an amplitude of 0 V, while the Lagrange multiplier p has homogeneous Dirichlet boundary conditions. Additionally, a homogeneous Neumann boundary condition is utilized for the magnetic vector potential $\hat{\boldsymbol{A}}$.

- At Γ_{Air}: Homogeneous Neumann boundary conditions are imposed on $\hat{\varphi}$, p, and $\hat{\boldsymbol{A}}$.

By enforcing these boundary conditions, we ensure that the current flowing through both wires has the same magnitude and direction. The current flows from Γ_1 to Γ_3 and from Γ_2 to Γ_4. As a result, the magnetic flux density inside the choke is doubled due to the simultaneous current flow in both wires of equal magnitude. This allows us to determine the impedance of the choke as follows:

$$Z_{\mathrm{CM}} = \frac{\hat{\varphi}_{\Gamma_1} - \hat{\varphi}_{\Gamma_3}}{I_{\Gamma_1} + I_{\Gamma_2}}. \tag{5.1}$$

For the DM case it is applied the following boundary condition:

- At Γ_1, the electric scalar potential $\hat{\varphi}$ is subject to inhomogeneous Dirichlet boundary conditions with an amplitude of 2 V. At the same time, the Lagrange multiplier p is subject to homogeneous Dirichlet boundary conditions. The magnetic vector potential $\hat{\boldsymbol{A}}$ is subject to a homogeneous Neumann boundary condition.
- At Γ_2, the electric scalar potential $\hat{\varphi}$ is subject to inhomogeneous Dirichlet boundary conditions with an amplitude of 0 V, while the Lagrange multiplier p is under homogeneous Dirichlet boundary conditions. The magnetic vector potential $\hat{\boldsymbol{A}}$ has a homogeneous Neumann boundary condition applied.
- At Γ_3 and Γ_4, we define inhomogeneous Dirichlet boundary conditions for the electric scalar potential $\hat{\varphi}$ with an amplitude of 1 V. Meanwhile, we define homogeneous Dirichlet boundary conditions for the Lagrange multiplier p. A homogeneous Neumann boundary condition is also applied to the magnetic vector potential $\hat{\boldsymbol{A}}$.
- At Γ_{air}: Homogeneous Neumann boundary conditions are imposed on $\hat{\varphi}$, p, and $\hat{\boldsymbol{A}}$.

By enforcing these boundary conditions, we ensure that the current flows through both wires of the same magnitude but in opposite directions. The current flows from Γ_1 to Γ_3 and from Γ_4 to Γ_2. Therefore, the magnetic flux density in the choke is compensated by the current flow in both wires with the same magnitude but in the opposite direction. The DM impedance Z_{DM} is expressed as:

$$Z_{\mathrm{DM}} = \frac{\hat{\varphi}_{\Gamma_1} - \hat{\varphi}_{\Gamma_2}}{I_{\Gamma_1}}. \tag{5.2}$$

5.2 CST Studio Suite®

CST Studio Suite [9] is utilized for simulating purposes, solving the complete set of Maxwell's equations as reference using the complex permeability. It is part of 3Dexperience and is not open-source like openCFS. The settings in CST vary from those in openCFS. The simulation employs low-frequency and high-frequency solvers with distinct settings to model the ferrite choke.

5.2.1 Low-Frequency Solver

The low-frequency frequency domain solver can simulate the electromagnetic fields excited by periodic low-frequency signals [10]. The CST is excited through the "Current Port", which determines the magnitude and direction of the flow on the surface (See Figure 5.2). Consequently, we define a current port with an amplitude 1 A at Γ_1, Γ_2, Γ_3, and Γ_4. The current flows in the same direction for CM (See Figure 5.2a), but in the opposite direction in the case of DM (See Figure 5.2b) The electric boundary condition $\boldsymbol{E} \times \boldsymbol{n} = \boldsymbol{0}$ is applied to all boundaries in CST.

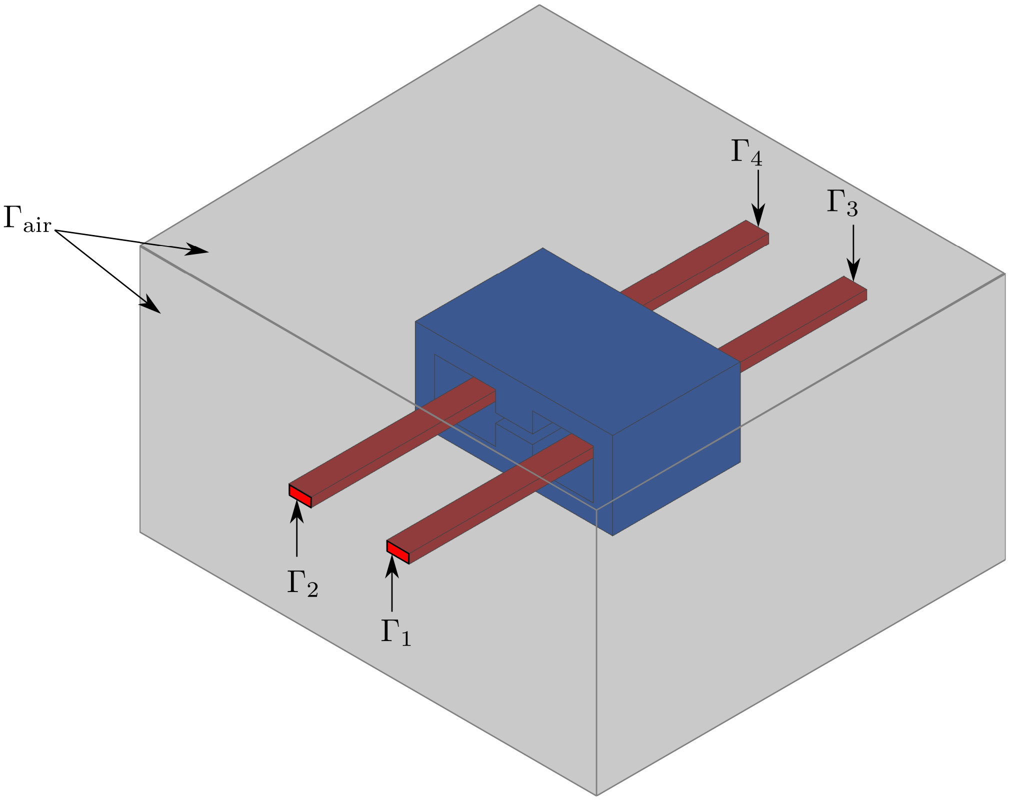
Γ_{air}
Γ_4
Γ_3
Γ_2
Γ_1

Figure 5.1: Boundary condition for Darwin model solver.

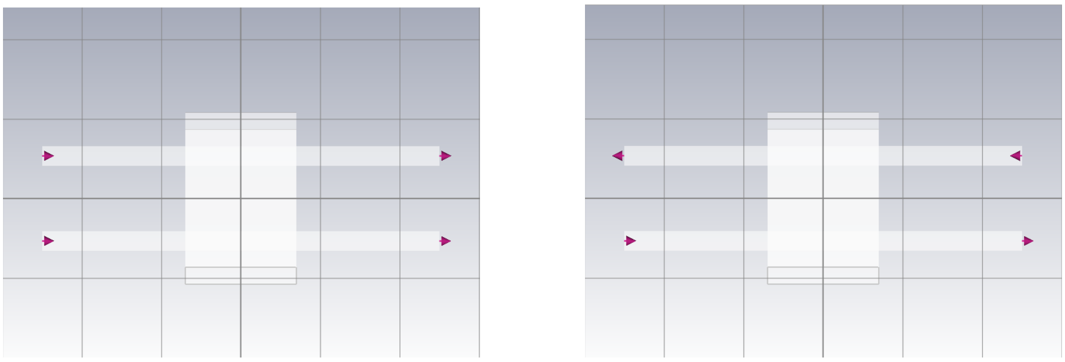

(a) *CM configuration.*

(b) *DM configuration.*

Figure 5.2: Current port in CST.

5.2.2 High-Frequency Solver

In the high-frequency solver, the choke is excited with discrete ports. Each port is connected at each end of the wire, illustrated in Figure 5.3. These discrete ports need grounding to create a closed circuit. The discrete port length is 12 mm to prevent the ferrite material from contacting the electric boundary condition $\boldsymbol{E} \times \boldsymbol{n} = \boldsymbol{0}$. All remaining boundaries are designated as open boundary conditions. The impedances for both the CM and DM are calculated through the use of S-parameters, which are discussed in [15]. These values are determined through mixed S-parameters for a four-port system, which can be represented by the matrix $\boldsymbol{S}$:

$$\boldsymbol{S} = \begin{bmatrix} S_{11} & S_{12} & S_{13} & S_{14} \\ S_{21} & S_{22} & S_{23} & S_{24} \\ S_{31} & S_{32} & S_{33} & S_{34} \\ S_{41} & S_{42} & S_{43} & S_{44} \end{bmatrix} \tag{5.3}$$

Additionally, a matrix $\boldsymbol{M}$ is introduced:

$$\boldsymbol{M} = \frac{1}{\sqrt{2}} \begin{bmatrix} 1 & -1 & 0 & 0 \\ 1 & 1 & 0 & 0 \\ 0 & 0 & 1 & -1 \\ 0 & 0 & 1 & 1 \end{bmatrix} \tag{5.4}$$

The mixed-mode S-parameters, denoted as $\boldsymbol{S}_{\mathrm{mm}}$, are then computed as follows:

$$\boldsymbol{S}_{\mathrm{mm}} = \boldsymbol{M}\boldsymbol{S}\boldsymbol{M}^{-1} \tag{5.5}$$

This mixed-mode S-parameter matrix, $\boldsymbol{S}_{\mathrm{mm}}$, can be further decomposed into submatrices:

$$\boldsymbol{S}_{\mathrm{mm}} = \begin{bmatrix} \boldsymbol{S}_{\mathrm{mm},11} & \boldsymbol{S}_{\mathrm{mm},12} \\ \boldsymbol{S}_{\mathrm{mm},21} & \boldsymbol{S}_{\mathrm{mm},22} \end{bmatrix} \tag{5.6}$$

Where each submatrix $\boldsymbol{S}_{\mathrm{mm,ij}}$ has the form:

$$\boldsymbol{S}_{\mathrm{mm,ij}} = \begin{bmatrix} S_{\mathrm{dd,ij}} & S_{\mathrm{dc,ij}} \\ S_{\mathrm{cd,ij}} & S_{\mathrm{cc,ij}} \end{bmatrix} \tag{5.7}$$

The following formula is used to calculate impedance:

$$Z = Z_0 \frac{(1 + S_{11})(1 + S_{11}) - S_{12}S_{21}}{2S_{21}} \tag{5.8}$$

The computation of the CM impedance is calculated as proposed in [15]. The reference impedance Z_0 is equal to 100 Ω and for the DM impedance the reference impedance is 25 Ω.

$$Z_{\mathrm{CM}} = 100 \frac{(1 + S_{cc,11})(1 + S_{cc,11}) - S_{cc,12}S_{cc,21}}{2S_{cc,21}} \tag{5.9}$$

$$Z_{\mathrm{DM}} = 25 \frac{(1 + S_{dd,11})(1 + S_{dd,11}) - S_{dd,12}S_{dd,21}}{2S_{dd,21}}. \tag{5.10}$$

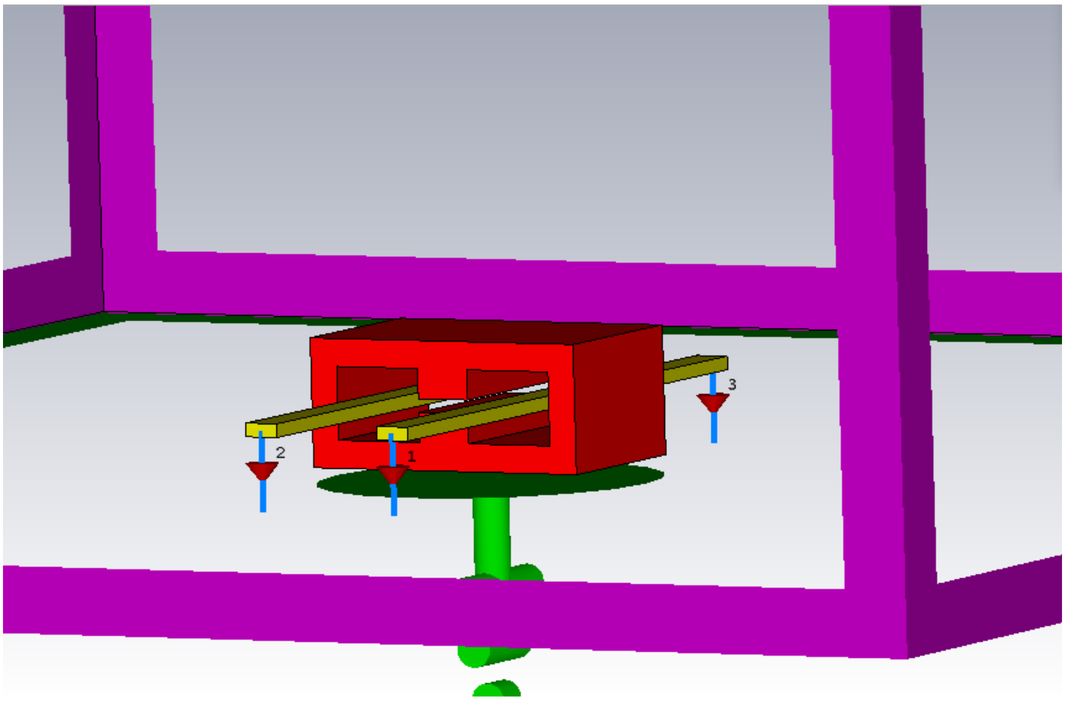

Figure 5.3: Discrete Port.

5.3 Results

This section presents results from solving Maxwell's equations using CST and applying the Darwin approximation with openCFS. Subsequently, we will extract equivalent circuit parameters, as discussed in Chapter 2, and compare them with the simulation results.

5.3.1 Common-Mode Choke

Figure 5.4, 5.5, and 5.6 demonstrate the CM choke impedance behavior across various frequencies using Fair-rite 75, Fair-rite 98, and TDK T37 ferrites, respectively. The frequency in Hz is represented on the x-axis, while the y-axis represents the magnitude of the CM impedance. The black curve shows the impedance solution from openCFS, the pink curve shows the solution from the CST low-frequency solver, the red curve shows the solution from the high-frequency solver, and the blue curve shows the solution of the equivalent circuit. The result from the Darwin model (openCFS) is in good agreement with the result of the CST HF solver, which solves the full set of Maxwell's equations. The CST LF solver deviates from openCFS and CST HF solver after 10MHz due to the electric boundary $\boldsymbol{E} \times \boldsymbol{n} = \mathbf{0}$ on all sides, which affects the impedance. The impedance increased linearly until 1 MHz and then begins to decrease. This can be explained by the fact that at low frequencies, the real part of the complex permeability is constant while the loss, i.e., the imaginary part, is very small compared to the real part. Therefore, it behaves as an inductance in the low-frequency range. The Darwin model and the full set of Maxwell's equations show similar results for each solver in the low-frequency range. However, the impedance starts to deviate beyond 1 MHz due to the behavior of the complex permeability, wherein the real component μ' decreases and the imaginary component μ'' increases. At 5 MHz, the impedance reaches maximum loss and then starts to decrease, resulting in reduced impedance.

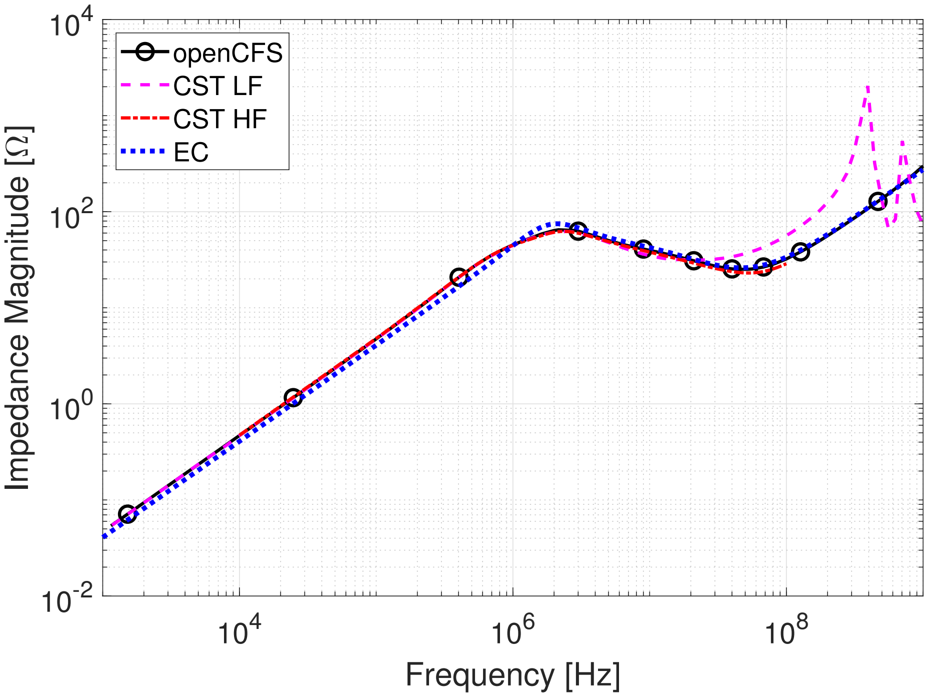

Figure 5.4: Impedance of the CM choke using Fair-rite 75.

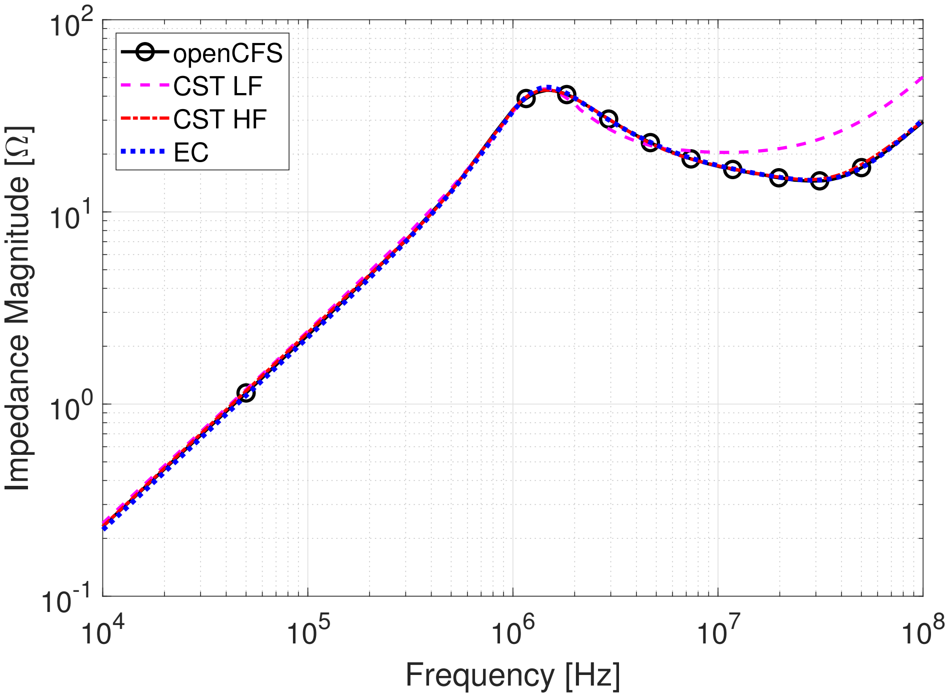

Figure 5.5: Impedance of the CM choke using Fair-rite 98.

Figure 5.7, 5.8 and 5.9 show the equivalent circuit of the common mode impedance for Fair-rite 75, Fair-rite 98 and TDK T37, respectively. The equivalent circuit was

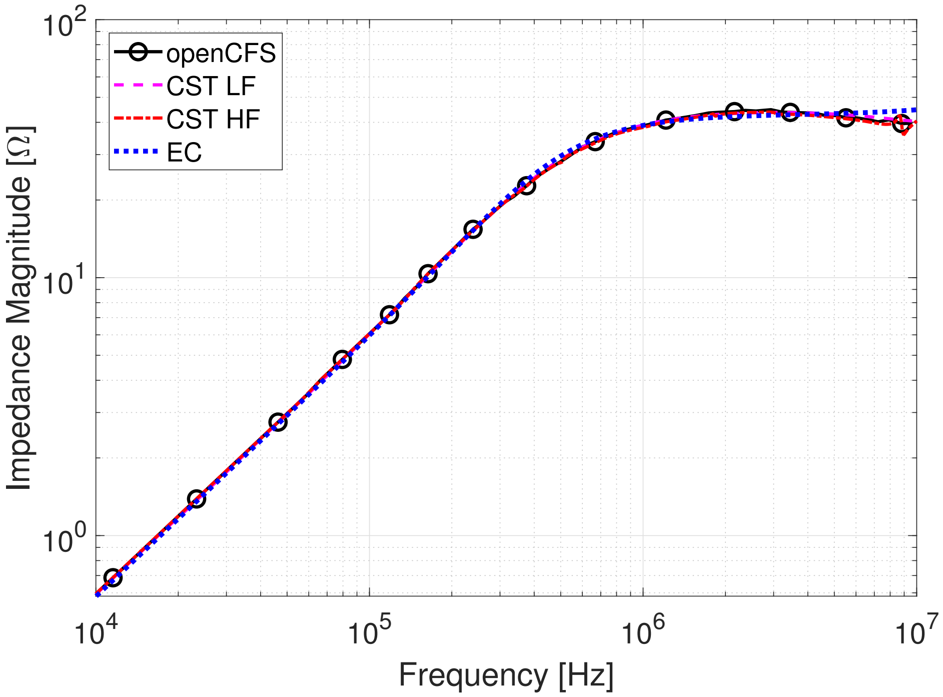

Figure 5.6: Impedance of the CM choke using TDK T37.

obtained from the Darwin model (openCFS). The common mode impedance for all three materials agrees excellently with the Darwin model (openCFS) results. The common mode impedance was calculated in admittance form, using $Y(s) = 1/Z(s)$. For Fair-rite 75, $m = n = 4$, where m is the order of the numerator $N(s)$ and n is the order of the denominator $D(s)$. For the Fair-rite 98, $m = n = 5$. For the TDK T37, $m = 2$ and $n = 3$. The Fair-rite 75 has four poles, two of then are real and one of which is a complex pair pole. One of the real poles has a negative residue r_i. It was discussed in the implementation of the extraction lumped element Section 2.3 that the RL circuit is converted into an RC in series with a parallel negative resistor R. This ensures that only the resistance is negative since the pole is stable ($p_i < 0$) rather than having both negative resistance and inductance. The same applies to Fair-rite 98 and TDK T37.

5.3.2 Differential-Mode Choke

Figure 5.10, 5.11 and 5.12 depict the impedance characteristics of Fair-rite 75, 98, and TDK T37, respectively, with respect to the DM impedance. Although the choke's magnetic field is compensated, there is still a leakage magnetic field that introduces a small inductor. Thus, the DM impedance for the three ferrites behaves as an inductor until 20 MHz, at which point it becomes slightly flatter before reaching a resonance frequency (as is the case with Fair-rite 75). The CST HF solver's result appears marginally higher compared to the others. A plausible explanation could be that the open boundary is insufficiently large for the lower frequency range.

Figure 5.13, 5.13 and 5.15 depict the equivalent circuit and its lumped element value. The Equivalent Circuit (EC)'s outcome exhibits remarkable agreement with the openCFS and CST LF, HF solver simulations. Fair-rite 75, executed with $m = 7$

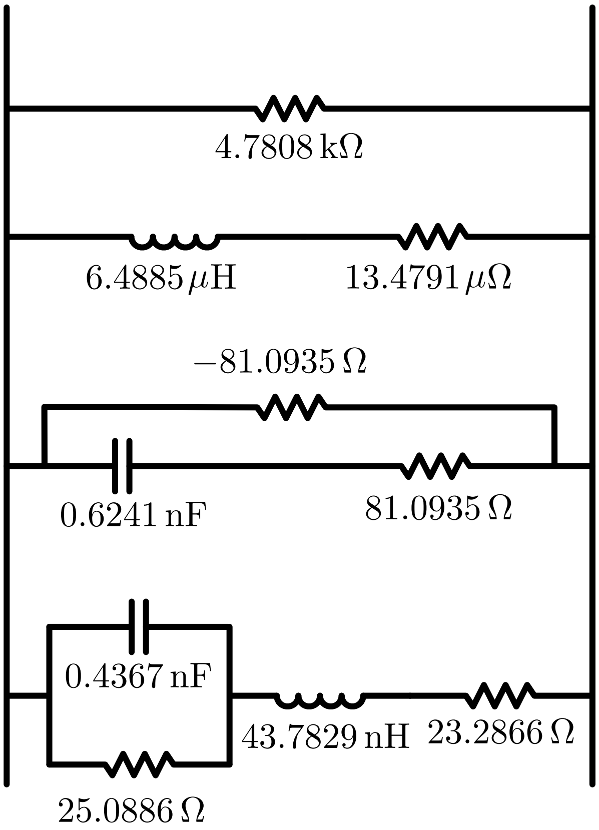

Figure 5.7: The equivalent circuit of the CM choke using Fair-rite 75.

and $n = 6$; Fair-rite 98, with $m = n = 5$; and TDK T37, with $m = 1$ and $n = 2$. Fair-rite 75 yields six real poles, with four having positive residue and two negative residue; whereas Fair-rite 98 has four poles, only two of them are real poles while the remaining two form a complex pole pair. One of the real poles possesses a negative residue. Therefore, a passivity test is necessary to determine whether the system is passive or not. TDK T37 possesses only 2 real poles with a positive residue.

5.3.3 Passivity

To check whether the transfer function $Y(s)$ is passive or not, two things need to be confirmed. The first one is the transfer function $Y(s)$ is stable, and the second one is the real part of the transfer function is positive for all frequencies [24]. The two conditions are as following:

- $\Re\{p_i\} < 0$ for all i.
- $\Re\{Y(j\omega) > 0\}$ for all frequencies $\omega > 0$.

Table 5.1 displays all poles of the fitting transfer function $Y(s)$ for the CM and DM cases. It can be observed that all poles are located on the left half plane, thereby satisfying the first condition. Additionally, Figure 5.16 depicts the characteristic behavior of the real component of $Y(s)$, covering frequency ranges from 0.01 Hz to 10 GHz. The frequency range from 0.01 Hz to 10 GHz shows a positive real component, indicating that the system is passive within these frequencies.

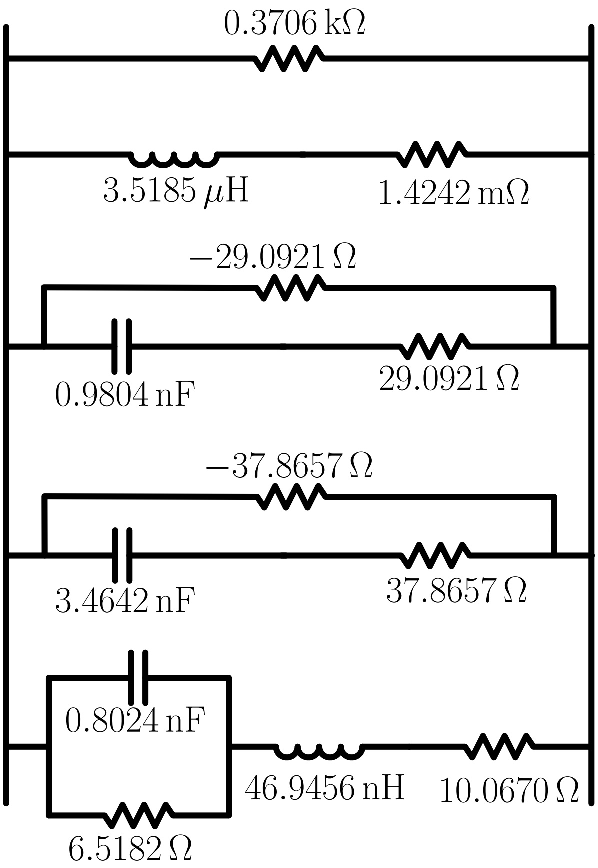
0.3706 kΩ
3.5185 μH
1.4242 mΩ
−29.0921 Ω
0.9804 nF
29.0921 Ω
−37.8657 Ω
3.4642 nF
37.8657 Ω
0.8024 nF
46.9456 nH
10.0670 Ω
6.5182 Ω

Figure 5.8: The equivalent circuit of the CM choke using Fair-rite 98.

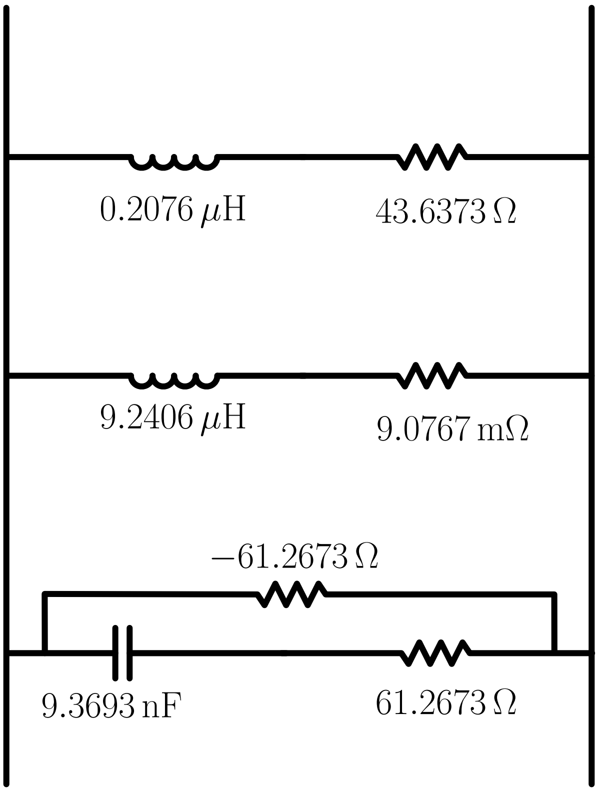
0.2076 μH
43.6373 Ω
9.2406 μH
9.0767 mΩ
−61.2673 Ω
9.3693 nF
61.2673 Ω

Figure 5.9: The equivalent circuit of the CM choke using TDK T37.

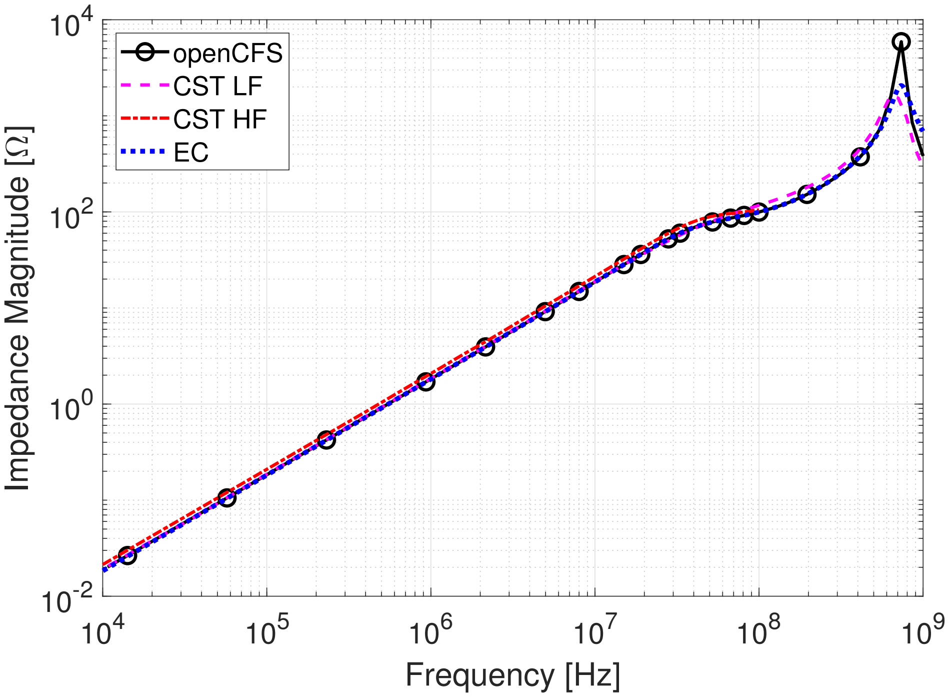

Figure 5.10: Impedance of the DM choke using Fair-rite 75.

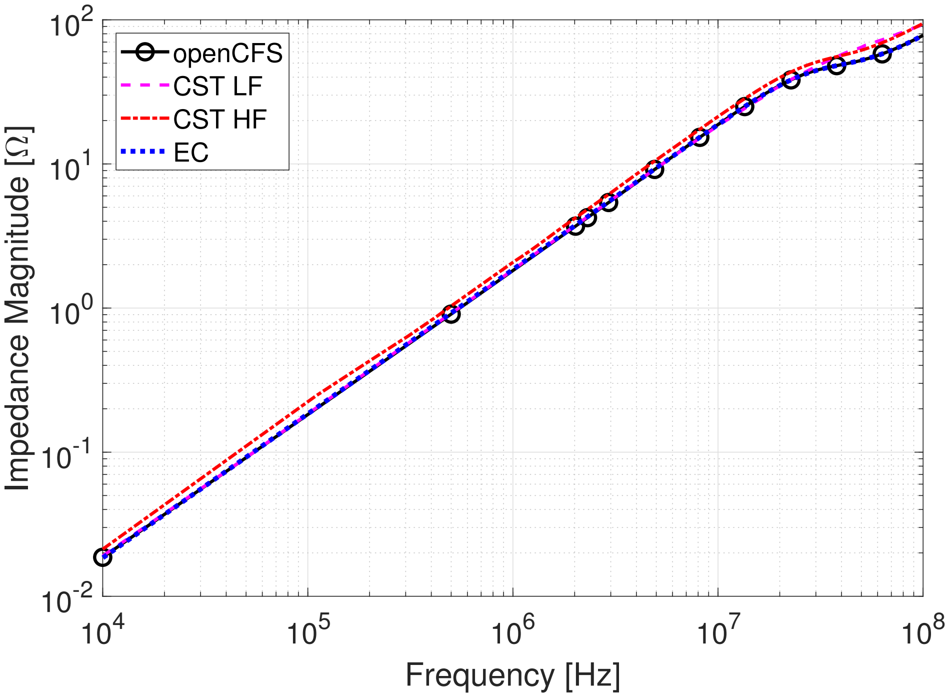

Figure 5.11: Impedance of the DM choke using Fair-rite 98.

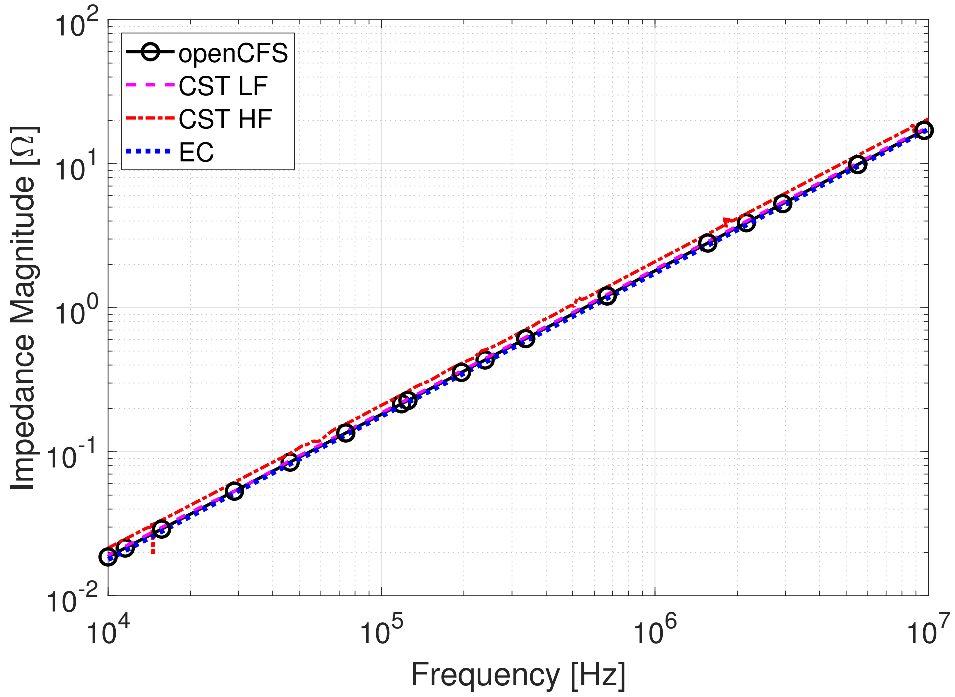

Figure 5.12: Impedance of the DM choke using TDK T37.

	Fair-Rite 75	Fair-Rite 98	TDK T37
CM	- 3.1157e+08 +i6.1402e+07	- 2.0282e+08 +i1.6252e+08	- 2.1017e+08
	- 3.1157e+08 -i6.1402e+07	- 2.0282e+08 -i1.6252e+08	- 1.7421e+06
	- 1.9758e+07	- 3.5063e+07	- 9.8226e+02
	- 2.0774e+00	- 7.6233e+06	
		- 4.0476e+02	
DM	- 7.5095e+08	- 2.6072e+08 +i1.3844e+08	- 8.0417e+05
	- 2.6339e+08	- 2.6072e+08 -i1.3844e+08	- 2.6368e+02
	- 3.2124e+06	- 1.7615e+07	
	- 2.5213e+07	- 2.2836e+03	
	- 2.4925e+05		
	- 5.7959e+02		

Table 5.1: Poles of the admittance $Y(s)$.

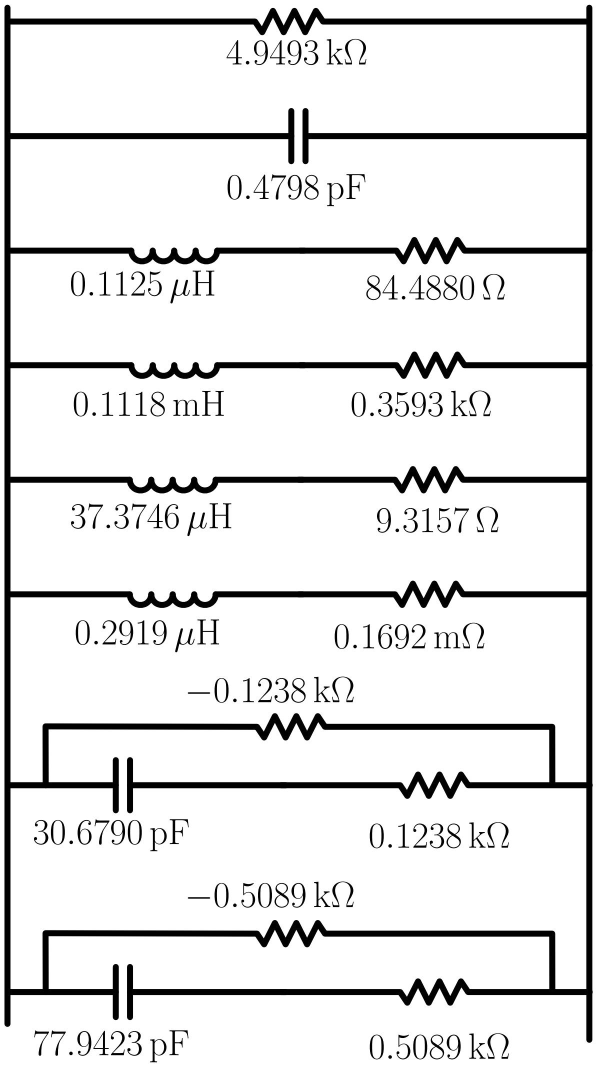
4.9493 kΩ
0.4798 pF
0.1125 μH
84.4880 Ω
0.1118 mH
0.3593 kΩ
37.3746 μH
9.3157 Ω
0.2919 μH
0.1692 mΩ
−0.1238 kΩ
30.6790 pF
0.1238 kΩ
−0.5089 kΩ
77.9423 pF
0.5089 kΩ

Figure 5.13: The equivalent circuit of the DM choke using Fair-rite 75.

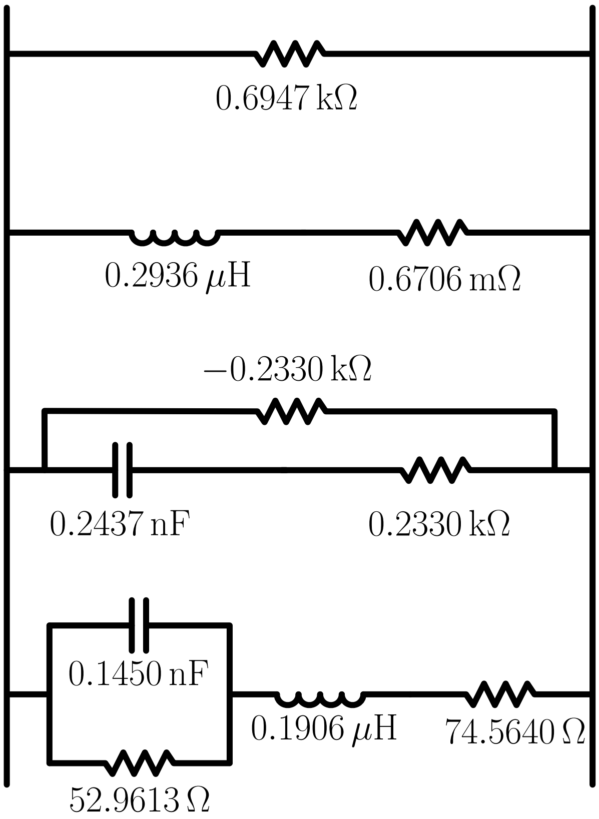
0.6947 kΩ
0.2936 μH
0.6706 mΩ
−0.2330 kΩ
0.2437 nF
0.2330 kΩ
0.1450 nF
0.1906 μH
74.5640 Ω
52.9613 Ω

Figure 5.14: The equivalent circuit of the DM choke using Fair-rite 98.

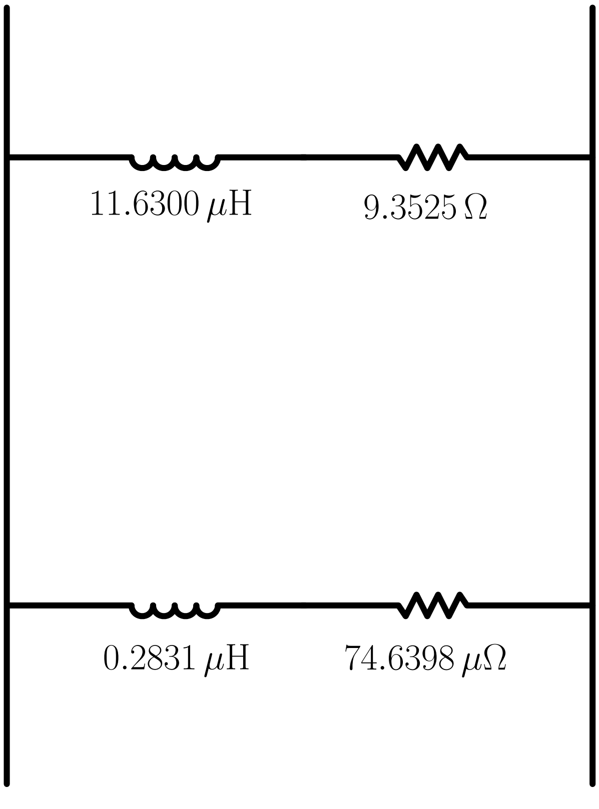
11.6300 μH
9.3525 Ω
0.2831 μH
74.6398 μΩ

Figure 5.15: The equivalent circuit of the DM choke using TDK T37.

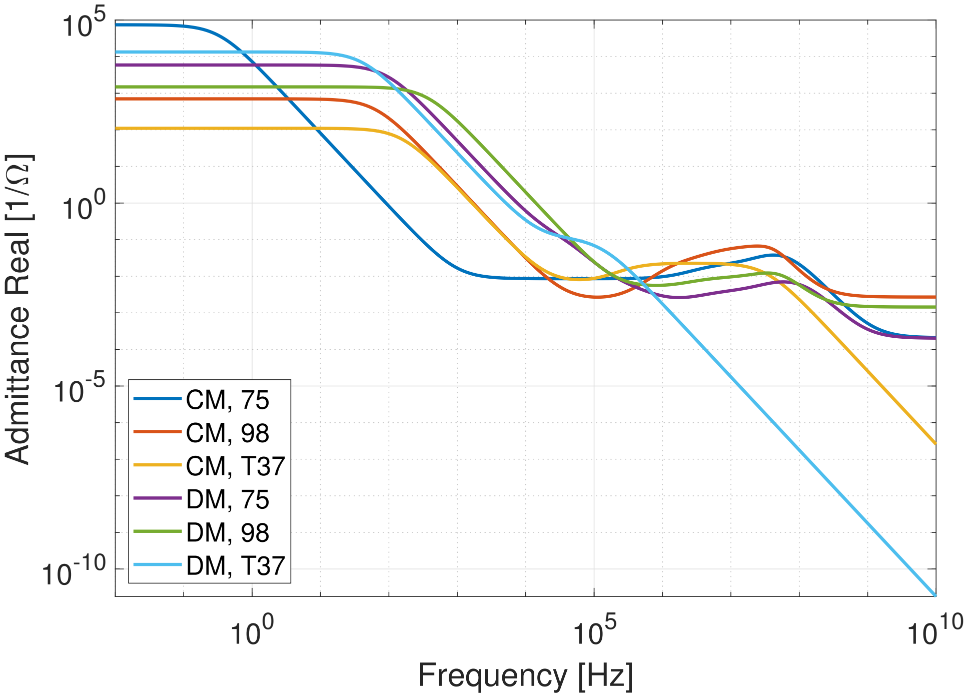

Figure 5.16: Real component of $Y(s)$.

Conclusion

Achievements

This thesis analyzes the Darwin approximation and its limitations concerning the full set of Maxwell's equations. We employ the FEM to solve the Darwin model and observe that the Darwin approximation result aligns well with the full set of Maxwell's equations when complex permeability is considered. We discuss an equivalent circuit based on a systematic method rather than a stochastic approach. The results obtained using the equivalent circuit (with IRFA) demonstrate a high correlation with those of the simulation employing the Darwin model. It is important to note that the equivalent circuit may contain negative lumped elements, warranting a passivity test to determine whether the whole system is passive. In cases where the system is non-passive, alternative configurations could be explored, such as increasing or decreasing the order of the nominator $B(s)$ and/or denominator $A(s)$. One can employ a passivity enforcement technique by adjusting the coefficients of $B(s)$ and $A(s)$ to ensure the system remains passive.

APPENDIX
A

Appendix A

Assume we have an Linear-Time-Invariant system (LTI) $Z(s)$ with an input $u(t)$ and an output $y(t)$

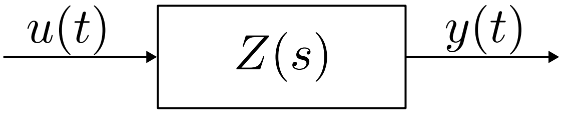

Figure A.1: Linear-Time-Invariant system.

$$\begin{aligned} Z(s) = \frac{Y(s)}{U(s)} &= \frac{b_m s^m + b_{m-1}s^{m-1} + ... + b_1 s + b_0}{s^n + a_{n-1}s^{n-1} + ... + a_1 s + a_0} \\ &= \frac{b_m s^m + b_{m-1}s^{m-1} + ... + b_1 s + b_0}{\prod_{i=1}^{n}(s - p_i)} \end{aligned} \tag{A.1}$$

A.1 Stability

A system $Z(s)$ is stable if the output $y(t)$ is bounded for all bounded inputs $u(t)$. Specifically, $Z(s)$ is considered stable if the real component of the roots of the denominator polynomial is less than zero. These roots are referred to as the poles p_i of $Z(s)$. If the real component of the poles exceed zero, the system is unstable. In the event that $\Re\{p_i\} = 0$, the system may either be unstable or marginally stable.

A.2 Passivity

Passivity is a property of a systems that describes their energy behavior. A passive system neither generates nor amplifies energy; instead, it either consumes or stores energy. For instance, resistors, capacitors, and inductors are called passive components. A system $Z(s)$ is passive if and only if:

1. $Z(\sigma)$ is purely real for σ real
2. $Z(s)$ is analytic for $\Re\{s\} > 0$
3. $\Re\{Z(j\omega)\} \geq 0$ for $\omega \in \mathbb{R}$

Condition (1) requires that each complex pole/residue pair appear with its conjugate, while (2) is satisfied if all poles are stable [24].

Appendix B

B.1 MATLAB code

```
Fs = 1./Z_meas;
s = 1j*2*pi*f_meas;
m = 4;
n = m;

N_max = 10;
N_iter = 0;
eps_iter = 100;
eps_max = 0.1;


[bn, an] = RFA(Fs,s,n,m);

Fsfit = zeros(size(s));
while eps_iter>eps_max && N_iter<N_max
        [Ks,Rs,Ps,an,bn] = IRFA(Fs,s,bn,an);
        unstables=real(Ps)>0;
        if ~isempty(unstables)
                Ps(unstables)=Ps(unstables)-1.1*
                   real(Ps(unstables)); %Forcing
                   unstable poles to be stable...
        end
        [bn,an] = residue(Rs,Ps,Ks);
        bn = bn(:);
        an = an(:);

        Fsfit = s.^(m:-1:0)*bn./(s.^(n:-1:0)*an);

        eps_iter = max(abs(Fs - Fsfit)./abs(Fs));
        N_iter = N_iter + 1;
end
```

RFA function [3]

```
function [bn, an] = RFA(Fs,s,n,m)

A = [s.^(m:-1:0), -Fs.*s.^(n:-1:1)];

Ar = real(A);  % Real part of matrix A
Ai = imag(A);  % Imaginary part of matrix A
br = real(Fs); % Real part of vector B
bi = imag(Fs); % Imaginary part of vector B

[Xmax Ymax] = size(Ar);

An = [Ar;Ai];
Bn = [br;bi];

% using QR decomposition
[Q,R2] = qr(An,0); % QR decomposition - Matrix Q
   and R of An
At = R2;           % It updates the matrix An
B = Q.'*Bn;        % It updates the vector Bn
for col = 1:Ymax
  Euclidian(col) = norm(At(:,col),2); % Euclidian
      norm
  At(:,col) = At(:,col)./Euclidian(col);
end
x = At\B; % Solution for the system (Ax = b)
x = x./Euclidian.'; % Real solution


bn = x(1:m+1);
an = [x(m+2:end);1];
```

IRFA function [3]

```
function [Ks,Rs,Ps,an,bn] = IRFA(Fs,s,bn,an)


        n = length(an)-1;
        m = length(bn)-1;


        A_s = s.^(n:-1:0)*an;
        B_s = s.^(m:-1:0)*bn;

        M = [s.^(m:-1:0), -Fs.*s.^(n:-1:1)];

        W1 = diag(1./(real(B_s./A_s)));
        W2 = diag(1./(imag(B_s./A_s)));
        Sigma = diag(1./A_s);
```

```
Ar = real(W1*Sigma*M);  % Real part of matrix A
Ai = imag(W2*Sigma*M);  % Imaginary part of
   matrix A
br = real(W1*Sigma*Fs); % Real part of vector B
bi = imag(W2*Sigma*Fs); % Imaginary part of
   vector B

[Xmax Ymax] = size(Ar);

An = [Ar;Ai];
Bn = [br;bi];



% using QR decomposition
[Q,R2] = qr(An,0); % QR decomposition - Matrix Q
   and R of An
At = R2;           % It updates the matrix An
B = Q.'*Bn;        % It updates the vector Bn
for col = 1:Ymax
        Euclidian(col) = norm(At(:,col),2); %
           Euclidian norm
        At(:,col) = At(:,col)./Euclidian(col);
end
x = At\B;   % Solution for the system (Ax = b)
x = x./Euclidian.'; % Real solution


bn = x(1:m+1);
an = [x(m+2:end); 1];
[Rs,Ps,Ks] = residue(bn,an);
```

Bibliography

[1] URL: https://fair-rite.com/.

[2] URL: https://www.tdk-electronics.tdk.com/.

[3] Eduardo Salvador Bañuelos-Cabral, José Alberto Gutiérrez-Robles, and Bjørn Gustavsen. “Rational Fitting Techniques for the Modeling of Electric Power Components and Systems Using MATLAB Environment”. In: *Rational Fitting Techniques for the Modeling of Electric Power Components and Systems Using MATLAB Environment*. Ed. by Eduardo Salvador Banuelos-Cabral, Jose Alberto Gutierrez-Robles, and Bjorn Gustavsen. Rijeka: IntechOpen, 2017. Chap. 1. DOI: 10.5772/intechopen.71358. URL: https://doi.org/10.5772/intechopen.71358.

[4] Javad Borsalani, Ali Dastfan, and Javad Ghalibafan. “An Integrated EMI Choke With Improved DM Inductance”. In: *IEEE Transactions on Power Electronics* 36.2 (2021), pp. 1646–1658. DOI: 10.1109/TPEL.2020.3010131.

[5] Henglin Chen, Zhaoming Qian, Shaodong Yang, and Christian Wolf. “Finite-Element Modeling of Saturation Effect Excited by Differential-Mode Current in a Common-Mode Choke”. In: *IEEE Transactions on Power Electronics* 24.3 (2009), pp. 873–877. DOI: 10.1109/TPEL.2008.2010126.

[6] Markus Clemens, Marvin-Lucas Henkel, Fotios Kasolis, Michael Günther, Herbert De Gersem, and Sebastian Schöps. “Electromagnetic Quasistatic Field Formulations of Darwin Type”. In: *ArXiv* abs/2204.06286 (2022). URL: https://api.semanticscholar.org/CorpusID:248157422.

[7] Markus Clemens, Bernhard Kähne, and Sebastian Schöps. “A Darwin Time Domain Scheme for the Simulation of Transient Quasistatic Electromagnetic Fields Including Resistive, Capacitive and Inductive Effects”. In: *2019 Kleinheubach Conference*. 2019, pp. 1–4.

[8] *Coupled Field Simulation (openCFS)*. URL: https://opencfs.org.

[9] *CST STUDIO SUITE ELECTROMAGNETIC FIELD SIMULATION SOFTWARE*. URL: https://www.3ds.com/products-services/simulia/products/cst-studio-suite/.

[10] *CST Studio Suite Help*. URL: https://space.mit.edu/RADIO/CST_online/general/welcome_de.htm.

[11] Pierre Degond and P. A. Raviart. “An analysis of the Darwin model of approximation to Maxwell’s equations”. In: 1992. URL: https://api.semanticscholar.org/CorpusID:119902009.

[12] Hiroyuki Kaimori, Takeshi Mifune, and Akihisa Kameari. “Investigation of Darwin Model with Two Types of Coulomb Gauge Condition in Frequency-Domain Electromagnetic Finite-Element Method”. In: *Progress in Industrial Mathematics at ECMI 2021*. Ed. by Matthias Ehrhardt and Michael Günther. Cham: Springer International Publishing, 2022, pp. 463–469. ISBN: 978-3-031-11818-0.

[13] Manfred Kaltenbacher. *Numerical simulation of mechatronic sensors and actuators: Finite elements for computational multiphysics, third edition.* Jan. 2015, pp. 1–587. ISBN: 978-3-642-40169-5. DOI: `10.1007/978-3-642-40170-1`.

[14] S. Koch and T. Weiland. “Different types of quasistationary formulations for time domain simulations”. In: *Radio Science* 46.5 (2011). DOI: `https://doi.org/10.1029/2010RS004637`. eprint: `https://agupubs.onlinelibrary.wiley.com/doi/pdf/10.1029/2010RS004637`. URL: `https://agupubs.onlinelibrary.wiley.com/doi/abs/10.1029/2010RS004637`.

[15] Konstantin Kostov and Jorma Kyyra. “Common-mode choke coils characterization”. In: *2009 13th European Conference on Power Electronics and Applications*. 2009, pp. 1–9.

[16] Hong Li, Chao Feng, Zhichang Yang, and Zhichao Yang. “An improved ferrite choke RLC model and its parameters determination method”. In: *IECON 2017 - 43rd Annual Conference of the IEEE Industrial Electronics Society*. 2017, pp. 6995–6999. DOI: `10.1109/IECON.2017.8217223`.

[17] Niek Moonen, Robert Vogt-Ardatjew, Anne Roc’h, and Frank Leferink. “3-D Full-Wave High Frequency Common Mode Choke Modeling”. In: *IEEE Transactions on Electromagnetic Compatibility* 62.3 (2020), pp. 707–714. DOI: `10.1109/TEMC.2019.2914371`.

[18] Richard Ozenbaugh and Timothy Pullen. *EMI filter design: Third edition*. Dec. 2017, pp. 1–272. ISBN: 9781315217116. DOI: `10.1201/b11543`.

[19] Nikolajs Ponomarenko. “Study of frequency and microstructure dependencies of magnetic losses of ferrite materials and components”. In: *Riga Technical University* (2014).

[20] K. Roppert, S. Kvasnicka, C. Riener, T. Bauernfeind, and M. Kaltenbacher. “Investigating Voltage Excitation of the Darwin Model via the Prescription of Terminal Scalar Potentials”. In: *IEEE Transactions on Magnetics* 58.9 (2022), pp. 1–4. DOI: `10.1109/TMAG.2022.3178139`.

[21] C. Sanathanan and J. Koerner. “Transfer function synthesis as a ratio of two complex polynomials”. In: *IEEE Transactions on Automatic Control* 8.1 (1963), pp. 56–58. DOI: `10.1109/TAC.1963.1105517`.

[22] Stanislav Skibin and Ivica Stevanović. “Behavioral circuit modeling of chokes with multi-resonances using genetic algorithm”. In: *2011 IEEE International Symposium on Electromagnetic Compatibility*. 2011, pp. 454–458. DOI: `10.1109/ISEMC.2011.6038354`.

[23] Wenhua Tan, Carlos Cuellar, Xavier Margueron, and Nadir Idir. “A High Frequency Equivalent Circuit and Parameter Extraction Procedure for Common Mode Choke in the EMI Filter”. In: *IEEE Transactions on Power Electronics* 28.3 (2013), pp. 1157–1166. DOI: `10.1109/TPEL.2012.2209206`.

[24] C. Walkey, D. Paul, M. S. Nakhla, R. Achar, and A. Weisshaar. “A novel passivity verification and enforcement algorithm for macromodels of microwave devices”. In: *2008 IEEE MTT-S International Microwave Symposium Digest*. 2008, pp. 611–614. DOI: `10.1109/MWSYM.2008.4633240`.

[25] Holger Wendland. “Direct Methods for Solving Linear Systems”. In: *Numerical Linear Algebra: An Introduction*. Cambridge Texts in Applied Mathematics. Cambridge University Press, 2017, 59–100. DOI: `10.1017/9781316544938.004`.

[26] Yanpu Zhao and Zuqi Tang. “A Novel Gauged Potential Formulation for 3-D Electromagnetic Field Analysis Including Both Inductive and Capacitive Effects”. In: *IEEE Transactions on Magnetics* 55.6 (2019), pp. 1–5. DOI: `10.1109/TMAG.2019.2899288`.